

## PROPELLER FORCES AND STRUCTURAL RESPONSE DUE TO CRASHBACK

**Peter A. Chang, III\***  
**Michael Ebert**

Ship Hydromechanics Directorate  
Naval Surface Warfare Center  
West Bethesda, MD 20817-5700  
Email: peter.chang@navy.mil

**Yin L. Young**  
**Zhanke Liu**

Dept. of Civil and Environmental Eng'g  
Princeton University, Princeton, NJ 08544  
Email: yyoung@princeton.edu

**Krishnan Mahesh**  
**Hyunchul Jang**

Aerospace Eng'g & Mechanics Dept.  
University of Minnesota  
Minneapolis, MN, USA 55455

**ENS Matthew Shearer<sup>†</sup>**  
U.S. Navy

### ABSTRACT

This work represents further progress in determining the fluid dynamic cause and effect between the highly turbulent flow features generated by crashback and the surface pressure loadings that these flows exert on the propeller. In addition, structural stresses, strains and deflections are predicted using these pressures. The data for these investigations is generated by large eddy simulations (LES) of a zero skew, 0.3048 m diameter model propeller 4381 run at a range of advance ratios. Statistics, probability density functions and power spectral density functions of the integrated forces on the blades are shown to compare well with water tunnel and open water experimental data. Using the 3-D and transient databases generated by the LES the physics of high-amplitude loading events have been investigated. It has been found that at low negative advance ratios, the flow is bimodal with vortex ring and axial jet modes, the latter of which occurs during the highest loadings. At higher negative advance ratios the flow remains in a ring vortex mode, though oscillations and asymmetries in the ring vortex are responsible for high am-

plitude loading events. Transient structural analyses of the propeller blade at the two  $J$  values, during low- and high-amplitude loading events are shown.

### 1 INTRODUCTION

A marine vehicle's ability to stop quickly and safely, without damage to itself or injury to its crew, is a major factor in determining its safe operating envelope. Crashback, used for emergency decelerations, is the maneuver where a forward-moving marine vehicle reverses its propeller, providing forward-directed thrust for maximum deceleration. Large blade loadings and unpredictable yaw and pitch moments can occur during this maneuver. The in-plane (or "side") forces act at a considerable distance from the center of lateral resistance and therefore, have the potential to impart large moments on the marine vehicle.

Some of the first crashback experiments, conducted in 1971, measured thrust and torque on Naval Surface Warfare Center — Carderock Division (NSWCCD) Propeller 4381 during crashback in open water.<sup>a</sup> Crashback experiments using laser sheet

---

\*Address all correspondence to this author.

<sup>†</sup>Formerly U.S. Naval Academy Trident Scholar, currently serving aboard CG 70.

---

<sup>a</sup>Experimental data provided courtesy of Code 5800, NSWCCD, West Bethesda, MD. These experiments will be referred to as open water or OW.  
Copyright © 2008 by ONR

visualization and particle displacement velocimetry (PDV) on Propeller 4381 in the NSWCCD 24-inch variable pressure water tunnel (VPWT) were performed by Jiang, Dong, Liu and Chang<sup>10</sup>. They concluded from their experiments, conducted at  $J = -0.472$  and  $J = -0.732$ , that the axial oscillations of the vortex ring and the high amplitude (HA) force events occurred at a non-dimensional frequency  $\omega D/U = 0.5$ , where  $\omega$  is the propeller rotation rate in radians/second,  $J = U/(nD)$  is the advance ratio,  $U$  is the free stream velocity,  $n$  is the propeller rotation rate in revolutions/sec and  $D$  is the propeller diameter. Experiments by Jessup et al.<sup>8</sup> in the NSWCCD 36-inch VPWT measured two-dimensional, transient velocity fields, multi-component forces and blade root strains for Propeller 4381 operating over a wide range of crashback advance ratios. Their PIV data shows that at  $J = -0.5$  the axial position of the vortex ring is highly unstable with macro-flow configurations ranging from a ring vortex centered near the blade tips to an elongated elliptical vortex upstream of the propeller. Jessup et al.<sup>9</sup> performed crashback experiments on a ducted propulsor configuration determining that the duct exacerbates the side forces. Dynamic crashback experiments, where  $J$  is varied to simulate realistic crashback evolutions, have been performed at NSWCCD's William B. Morgan Large Cavitation Channel (LCC) by Bridges.<sup>3</sup>

With the propeller forcing fluid forward into the oncoming flow a recirculating flow is setup in which the propeller, now rotating backwards, will be subject to large angles of attack (AOA). The leading and trailing edges of the propeller blades exchange roles and the typically sharp trailing edge now becomes the leading edge.<sup>b</sup> In combination with the large AOA the potential for large flow separations is very high and it is these separations that are ostensibly the cause of high amplitude load fluctuations. In theory, large eddy simulations (LES) are the optimal computational methodology for predicting the fluctuating forces generated in crashback. Reynolds-averaged Navier-Stokes (RANS) methods can obtain the correct mean forces during crashback, but fail to predict the fluctuating forces. LES, on the other hand, solve the equations of fluid motion, resolving, rather than modeling the most energetic scales of turbulence. The smallest (sub-grid) scales of turbulence are parameterized in a relatively simple sub-grid scale (SGS) model. However, because of the complexity of propeller geometries, resort must be made to LES in unstructured or overset grid frameworks.<sup>21</sup> Mahesh, Constantinescu, and Moin<sup>19</sup> report the development of a finite volume LES code, which is robust at high Reynolds number on arbitrary element, highly distorted, unstructured grids. Results of a crashback simulation on Propeller 4381 at  $J = -0.7$  using this code have been reported in Vysöhlíd and Mahesh.<sup>23,24</sup> Comparison to an unstructured, upwind-biased, finite volume LES code in crashback is documented in Chang, Mahesh and Shipman.<sup>4</sup>

<sup>b</sup>In this paper, the leading edge of the propeller will refer to the aft edge of the propeller, that which leads the blade when the propeller is rotated in reverse

There are a number of studies related to fluid structure interaction (*FSI*) analysis of marine propellers,<sup>11,2,15,16,17,12,14</sup> which focused either on steady or wetted conditions. A recent study by Lin and Tsai<sup>18</sup> investigated the free vibrations of propeller blades using an added mass formulation. It was found that the natural frequencies of the blade in water is much lower than those in air, which is consistent with the findings presented in Young<sup>25</sup>. Methodologies presented in Young<sup>25,26</sup> represent a comprehensive and state-of-the-art *FSI* analysis for flexible marine propellers during forward operations. The methodologies feature an unsteady boundary element method (*BEM*) fluid solver, an unsteady finite element method (*FEM*) solid solver, and an efficient coupling scheme. Spatially uniform and non-uniform wake inflows can be simulated. Both face and back side cavitations can be simultaneously captured. Isotropic and anisotropic materials can be modeled. Despite the advance of *FSI* modeling, most previous efforts focused on forward operations. For crashback operations, the fluid field features large scale turbulence, which imposes enormous challenges on the fully coupled *FSI* analysis. There is still a lack of unsteady structural analyses of marine propellers subject to crashback loading in the literature. Based on the fact that the structural deformation is small, a decoupled structural analysis is performed in the current work, which for the first time reveals the unsteady crashback response characteristics of propeller blades.

This paper first describes the mathematical formulations for the LES and structural analysis tools. This is followed by comparisons of statistics, probability density functions (PDF) and power spectral densities (PSD) of the integrated force time histories with experimental data. Then, the physics of high amplitude (HA) loading events at  $J = -0.5$  and  $J = -1$  are shown and finally the results of structural analysis at the high- and low-amplitude loading for the two  $J$ 's are shown.

## 2 PROPELLER SIMULATION DETAILS

### 2.1 Numerical Method

Simulations are performed in a rotating frame of reference using a LES code documented in Mahesh et al.<sup>19</sup> in a form where the system rotation generates a source term as in Majety<sup>20</sup>:

$$\frac{\partial u_i}{\partial t} + \frac{\partial}{\partial x_j} (u_i u_j - u_i \epsilon_{jkl} \omega_k x_l) = \frac{\partial p}{\partial x_i} - \epsilon_{ijk} \omega_j u_k + \nu \frac{\partial^2 u_i}{\partial x_j \partial x_j} \quad (1)$$

$$\frac{\partial u_i}{\partial x_i} = 0. \quad (2)$$

Here  $u_i$  is the velocity in the inertial frame of reference,  $p$  is the pressure,  $x_i$  are the coordinates in the moving frame of reference,  $t$  is the time,  $\omega$  is the angular velocity of the rotating frame of reference, and  $\nu$  is the kinematic viscosity. Note that the density is absorbed into the pressure. Also, the Einstein summation

convention is used and  $\varepsilon_{ijk}$  denotes the permutation symbol.

The LES equations are obtained by spatially filtering the Navier-Stokes equations (1) assuming that the filtering operation commutes with the spatial and temporal derivatives. The source term is approximated by

$$\overline{u_i \varepsilon_{jkl} \omega_k x_l} \approx \overline{u_i} \varepsilon_{jkl} \omega_k x_l \quad (3)$$

giving

$$\frac{\partial \overline{u}_i}{\partial t} + \frac{\partial}{\partial x_j} (\overline{u}_i \overline{u}_j - \overline{u_i \varepsilon_{jkl} \omega_k x_l}) = \frac{\partial \overline{p}}{\partial x_i} - \varepsilon_{ijk} \omega_j \overline{u}_k + \nu \frac{\partial^2 \overline{u}_i}{\partial x_j \partial x_j} - \frac{\partial \tau_{ij}}{\partial x_j} \quad (4)$$

$$\frac{\partial \overline{u}_i}{\partial x_i} = 0. \quad (5)$$

where the overbar denotes spatial filtering and

$$\tau_{ij} = \overline{u_i u_j} - \overline{u}_i \overline{u}_j \quad (6)$$

is the modeled subgrid scale stress. The dynamic SGS Smagorinsky as proposed by Germano et al.<sup>5</sup> and modified by Lilly<sup>13</sup> is used to model the SGS stress.

Equations (4)-(6) are solved using a numerical method developed by Mahesh et al.<sup>19</sup> for incompressible flows on unstructured grids. The finite volume algorithm, derived to be robust with minimal numerical dissipation, stores the Cartesian velocities and pressure at the control volume (CV) centroids with the face-normal velocities stored independently at the centroids of the faces. A predictor-corrector approach is used where the predicted velocities at the CV centroids are first obtained then interpolated to obtain the face-normal velocities. The predicted face-normal velocity is projected such that continuity is discretely satisfied. This yields a Poisson equation for pressure which is solved by algebraic multi-grid<sup>6</sup> or conjugate gradient approaches. The pressure field is used to update the Cartesian CV velocities using a least-squares formulation which is essential for obtaining solutions on highly skewed grids. Time advancement is performed using an implicit Crank-Nicholson scheme. Chang et al.<sup>4</sup> compare the speedups for solving large problems on massively parallel compute clusters using CG and AMG methods.

The algorithm has been validated for a variety of flows including the temporal decay of isotropic turbulence (DIT), flow over a circular cylinder, flow in a coaxial combustor, flow in a gas turbine combustor,<sup>19</sup> and initial crashback validations.<sup>23,24</sup> The DIT results are very important as they show that the code has the minimally-dissipative numerical scheme that can give the correct Reynolds number dependence i.e., when increasing the Reynolds

number of the turbulence while keeping the grid density constant, the temporal decay rate without SGS model goes to zero as the grid no longer supports the increasingly smaller scales of turbulence responsible for decay. The practical ramification of this result is that relatively few grid points may be necessary to initiate and maintain turbulent vortices, possibly allowing for crashback simulations to be run with relatively coarse grids.

## 2.2 Computational Grid and Boundary Conditions

Figure 1, a photograph of NSWCCD Propeller 4381 in the 36-inch VPWT, shows the experimental setup of Jessup et al.<sup>8</sup> The flow exits a tunnel into a plenum chamber containing the propeller. Computations were performed on the 0.3048m diameter Propeller 4381 mounted on a cylindrical shaft, located within a cylindrical outer domain simulating the plenum in the 36-inch VPWT. As shown in the lateral cut plane, Figure 2, the tunnel wall has a diameter of 7.3D, and the inflow and outflow boundaries are located 5.8D and 7.9D upstream and downstream, respectively, from the propeller plane.



Figure 1. Photograph of Propeller 4381 in 36-inch VPWT.

The computational grid, shown in Figures 3 and 4, is comprised of prisms off the blade surfaces, tetrahedra filling a cylinder around the propeller, prisms upstream and downstream of the cylinder and hexahedral mesh elements filling the outer radii. The grid directly off the hub and fairwater consists of tetrahedra. The mesh was developed in Gambit and T-Grid at the University of Minnesota and consists of 13 million control volumes. The minimum grid spacing at the blade tips is 0.0017D with the first node located at 0.0017D from the wall. It is known *a priori*

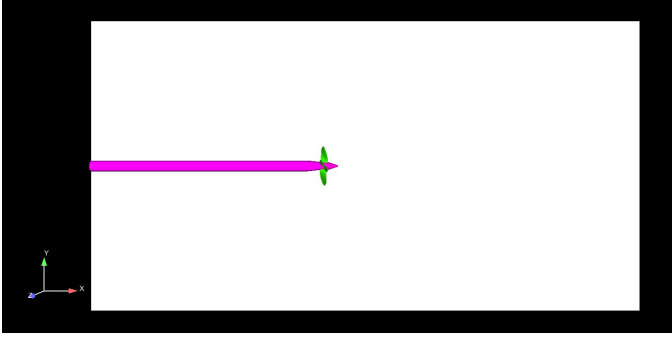


Figure 2. Lateral plane cut showing computational domain (white region). Freestream flow is from left to right.

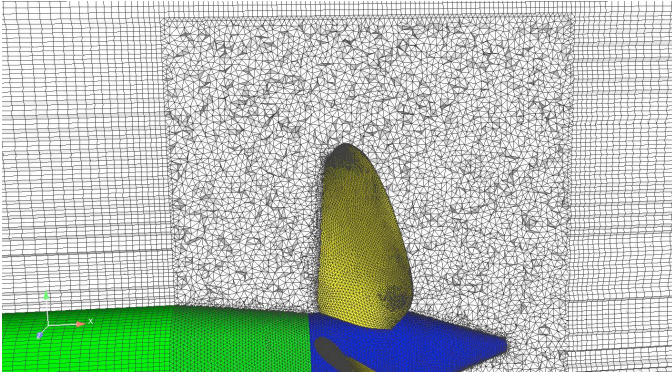


Figure 3. Close up view of computational grid

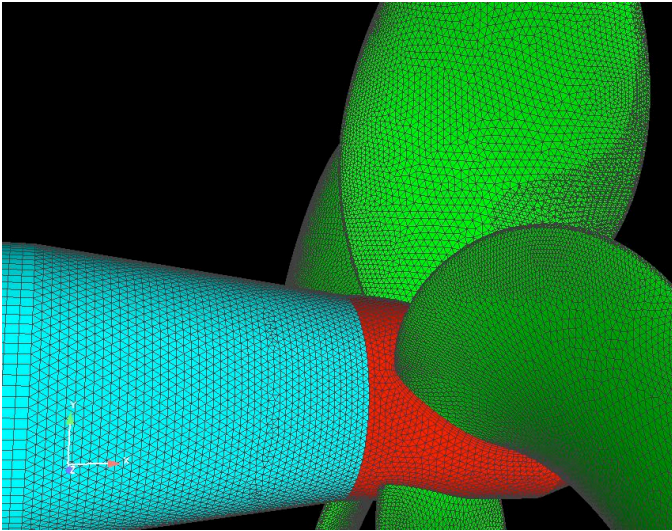


Figure 4. Propeller 4381 showing surface grid.

Table 1. Run conditions for simulations:  $U$  is the free stream velocity,  $L_R$  is the number of propeller revolutions run once the solution reached a statistically steady state.

$J$	$U$ (m/sec)	$L_R$
-0.3	1.067	370
-0.5	1.778	335
-0.7	2.489	302
-1.0	3.556	288

that this is relatively coarse wall normal spacing but the assumption (to be determined!) is that the dominant flows are highly separated *i.e.*, resolution of the viscous boundary layers may be of secondary importance for predicting high-amplitude loading. Even though the LES code solves the equations of fluid motion in a rotating frame of reference, the boundary conditions are applied in the inertial frame of reference. Therefore, on the blades, hub and fairwater  $\mathbf{v} = \boldsymbol{\omega} \times \mathbf{r}$  is specified (bold denotes vector quantities). The shaft surface is set to  $\mathbf{v} = (0, 0, 0)$  and the tunnel wall to  $\mathbf{v} = (U, 0, 0)$ . A constant velocity, zero turbulence kinetic energy boundary condition is set at the upstream boundary and a convective boundary condition is prescribed at the downstream boundary. Simulations documented in this paper were run using the 36-inch VPWT experimental conditions as reported in Jessup et al.<sup>8</sup> and are listed in Table 1 with  $\rho = 997.4 \text{ kg/m}^3$  and  $n = 700 \text{ rpm}$ .

The  $J = -0.5$  and  $J = -1.0$  simulations were performed on NSWCCD SEATech Center's SGI Altix computer and the  $J = -0.3$  and  $J = -0.7$  simulations were performed on the Blue Gene eServer at the San Diego Supercomputer Center.

### 2.3 Structural model

In this work, the propeller structural analysis is performed in the non-inertial blade-fixed coordinate system, which rotates with the reference blade. The discrete system of equations of the blade subject to the centrifugal force  $\{\mathbf{F}_{ce}\}$ , the Coriolis force  $\{\mathbf{F}_{co}\}$ , and the hydrodynamic force  $\{\mathbf{F}_r\}$  can be formulated as in Young<sup>25</sup>:

$$([\mathbf{M}] + [\mathbf{M}_H]) \{\ddot{\boldsymbol{\delta}}\} + ([\mathbf{C}] + [\mathbf{C}_H]) \{\dot{\boldsymbol{\delta}}\} + [\mathbf{K}] \{\boldsymbol{\delta}\} = \{\mathbf{F}\} \quad (7)$$

where  $\{\mathbf{F}\} = \{\mathbf{F}_{ce}\} + \{\mathbf{F}_{co}\} + \{\mathbf{F}_r\}$ ;  $\{\ddot{\boldsymbol{\delta}}\}$ ,  $\{\dot{\boldsymbol{\delta}}\}$ , and  $\{\boldsymbol{\delta}\}$  are the nodal acceleration, velocity, and displacement vectors, respectively;  $[\mathbf{M}]$ ,  $[\mathbf{C}]$ , and  $[\mathbf{K}]$  are the structural mass, damping, and stiffness matrices, respectively; and  $[\mathbf{M}_H]$  and  $[\mathbf{C}_H]$  are the

hydrodynamic added mass and hydrodynamic damping matrices, respectively. The influence of the hydrodynamic excitation is reflected in the hydrodynamic forcing term  $\{\mathbf{F}_r\}$ , which can be expressed in terms of the hydrodynamic pressure  $\{\mathbf{P}_r\}$  as  $\{\mathbf{F}_r\} = \int [\mathbf{N}]^T \{\mathbf{P}_r\} dS$ , where  $[\mathbf{N}]$  is the displacement interpolation matrix.

For the current problem of interest, the structural deformation due to turbulent crashback loading is small due to the high rigidity of the 12-inch diameter aluminum model scale propeller. Hence, the added mass and hydrodynamic damping effects are negligible so a decoupled hydroelastic analysis can be applied:

$$[\mathbf{M}] \{\ddot{\boldsymbol{\delta}}\} + [\mathbf{C}] \{\dot{\boldsymbol{\delta}}\} + [\mathbf{K}] \{\boldsymbol{\delta}\} = \{\mathbf{F}\} \quad (8)$$

The standard FEM package ABAQUS/Standard<sup>1</sup> is used to solve the unsteady decoupled structural response by applying the turbulent fluid loading from the LES solver as surface traction.

### 3 RESULTS

#### 3.1 Time Series

Figure 5 is the time history for  $J = -0.5$  showing the thrust, side force magnitude and the side force resultant direction. Thrust is defined as the force imparted by the fluid on the propeller blades in the axial direction, positive pointing aft; side force magnitude is the resultant of the fluid force components in the plane of the propeller; torque is the moment about the propeller centerline, positive pointing aft. The “K” coefficients are normalized in the traditional naval architecture manner:

$$K_T = \frac{T}{\rho n^2 D^4} \quad (9)$$

$$K_Q = \frac{Q}{\rho n^2 D^5} \quad (10)$$

$$K_S = \frac{\sqrt{F_y^2 + F_z^2}}{\rho n^2 D^4} \quad (11)$$

where a rotational velocity,  $nD$ , is used as the reference velocity and  $D^2$  is the reference area. The horizontal lines in Figure 5 are the mean and the mean plus 1, 2 and 3 standard deviations.  $K_T$  has one event that exceeds  $4\sigma$ , two events that exceed  $3\sigma$  and about six events that exceed  $2\sigma$ . The HA  $K_T$  events appear to be closely correlated with HA side force magnitude events. Figure 5(bottom) is the side force angle, defined as

$$\theta = \tan^{-1}(F_y/F_z). \quad (12)$$

It appears that during the HA side force events, at least where  $K_S > \overline{K_S} + 3\sigma$  the side force angle is relatively constant.

Table 2. Statistics for  $J = -0.5$ .

		LES	VPWT	OW
Mean	$K_T$	0.34	0.27	0.37
	$K_Q$	-0.64	-0.57	-0.71
	$K_S$	0.025	0.031	
Standard deviation	$K_T$	0.056	0.056	
	$K_Q$	0.010	0.011	
	$K_S$	0.014	0.017	

Figure 6 is a plot of the mean thrust and torque coefficients predicted by the LES compared with the experimental open water test values of Hecker and Remmers (1971) and the VPWT data of Jessup et al.<sup>8</sup> The trend with increasing negative  $J$  is for the coefficients to decrease in magnitude to a minimum around  $J = -0.5$  then to increase in magnitude monotonically as  $J$  becomes more negative. The LES  $K_T$  and  $K_Q$  results follow this trend matching better with the OW results.

Figure 7 is a plot of the mean side force magnitude as function of  $J$ . The VPWT data has a small peak at  $J = -0.3$ , decreases slightly at  $J = -0.5$ , and then increases as  $J$  becomes more negative. The LES data compare well with the VPWT data for the middle two  $J$  values  $J = -0.5$  and  $J = -0.7$ . However, for  $J = -0.3$  the data is lower than the VPWT data, matching more closely the OW data. At  $J = -1$  the LES data is higher than the VPWT data, but not close to the OW data.

Tables 2 and 3 list the temporal means and standard deviations (SD) for  $K_T$ ,  $K_Q$  and  $K_S$  for the LES and experiments for  $J = -0.5$  and  $J = -1$ , respectively. For  $J = -0.5$ , the standard deviation values compare very well with experiments. For  $J = -1$  the standard deviation values for the LES are higher than the experiments. It is not known whether the differences are due to the differences between the VPWT experiment conditions and the more open condition in the LES domain. Unfortunately, standard deviation data for the OW experiments was not available to compare with.

Figures 6 and 7 may indicate that the worst loadings occur as  $J$  becomes more negative. This may be a result of their normalization. In the experiments<sup>8</sup> and computations  $n$  was held constant while  $U$  was varied. Thus,  $J = -1$  has twice the inflow velocity as  $J = -0.5$ . If the inflow velocity,  $U$ , rather than  $nD$ , is used as the velocity scale then we obtain the thrust and torque coefficients,

$$C_T = \frac{T}{\frac{1}{2}\rho U^2 A_D} \quad (13)$$

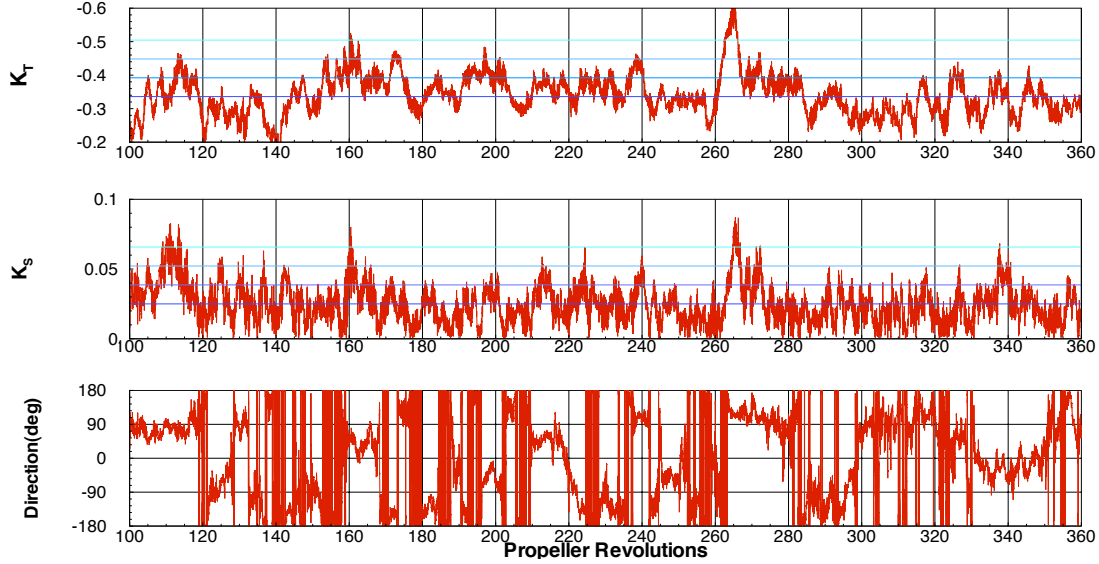


Figure 5. Time history for  $J = -0.5$ ; top:  $K_T$ , middle:  $K_S$  and bottom: side force angle. The blue horizontal lines are the mean,  $(\mu)$ ,  $\mu + \sigma$ ,  $\mu + 2\sigma$ , and  $\mu + 3\sigma$

Table 3. Statistics for  $J = -1$ .

		LES	VPWT	OW
Mean	$K_T$	-0.61	-0.53	-0.65
	$K_Q$	-0.111	-0.097	-0.116
	$K_S$	0.050	0.042	
Standard deviation	$K_T$	0.104	0.059	
	$K_Q$	0.019	0.010	
	$K_S$	0.030	0.022	

cient, for a constant AOA, is constant as flow speed is varied, implying that the kinematics of the flow about airfoil are the same with change in velocity. This hints at the notion for crashback that over a certain range of  $J$ , the thrust, and therefore, kinematics are invariant. In other words, over this range of  $J$ , the kinematics of the recirculation region are the same. For  $J > -0.6$  the force coefficients increase sharply such that it is possible that the propeller can exert an axial pressure equal to more than 20 times the stagnation pressure. In this range, the thrust coefficient varies rapidly with  $J$  (or inflow velocity), indicating that the kinematics (and AOA) are varying rapidly. In this paper we closely examine two cases,  $J = -0.5$  and  $J = -1$ , which may span the range of behaviors.

$$C_Q = \frac{T}{\frac{1}{2}\rho U^2 A_D^2} \quad (14)$$

where  $A_D$  is the propeller disk area. Figure 8 shows that  $C_T$  and  $C_Q$  are highest at small low negative  $J$ , becoming almost flat as  $J$  becomes more negative — a trend almost opposite that for forces normalized as per (9). Figure 9 shows that side force magnitude has the same trend. In other words, for  $J < -0.6$  the forces, and therefore, the flow physics, scale as the inflow velocity squared which is typical for airfoils in turbulent flow. In this range the propeller exerts an axially directed pressure equal to approximately twice the inflow stagnation pressure. For attached airfoil flows, the lift (or thrust) coefficient normalized similarly, is a function of the AOA. In a turbulent flow regime the lift coeffi-

### 3.2 Probability Distribution Functions and Maximum Loadings

Our interest lies in our ability to predict the HA propeller loading that will have the greatest effect on blade deformations and coursekeeping. It has been shown in the previous section that the LES predicts the mean forces and standard deviation reasonably well. However it is important to know if the LES can predict the highest loadings and the proportion of the time that these highest loadings occur. Probability density functions (PDFs) show the proportion of time that a certain force spends above or below a certain threshold. Figure 10 is the thrust PDF for the four  $J$  values simulated compared with VPWT experiment data. The experimental distributions are all Gaussian. The means are consistent with Figure 6(a) where the LES mean  $K_T$

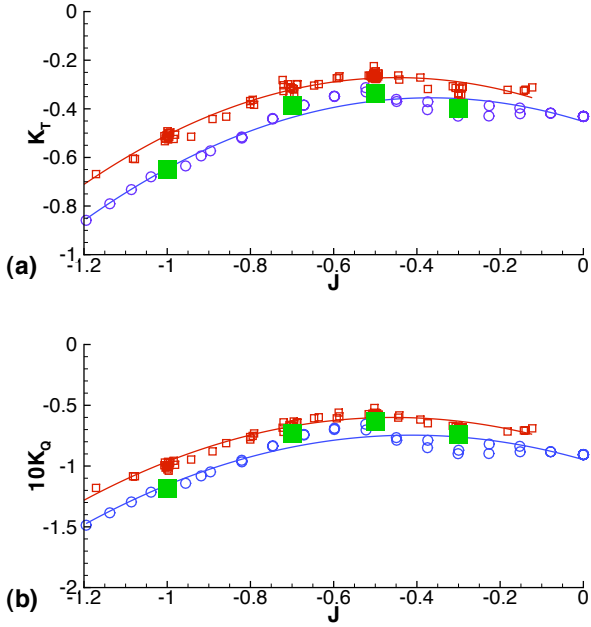


Figure 6. Mean propeller forces (a) thrust (b) torque.  $\circ$  : Open water;  $\square$  : VPWT<sup>8</sup>,  $\blacksquare$  : LES.

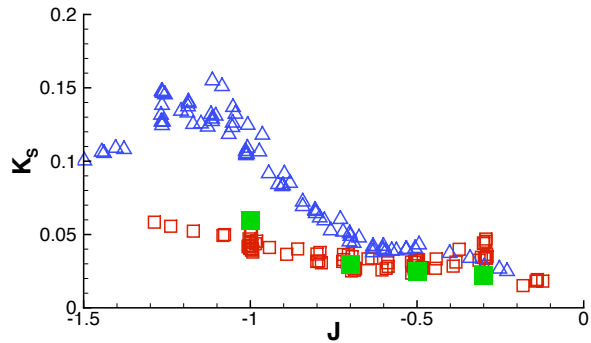


Figure 7. Mean propeller side force magnitude.  $\triangle$  : Open water;  $\square$  : variable pressure water tunnel (VPWT) results from Jessup et al.<sup>8</sup>,  $\blacksquare$  : LES.

are consistently lower than the VPWT data, but higher than the OW data. For  $J = -0.5$  and  $J = -0.7$  the LES and VPWT shapes are the same, consistent with the fact that the standard deviation are close, as demonstrated for  $J = -0.5$  in Table 2. The  $J = -0.3$  LES distribution has close to a Gaussian distribution but is double-peaked. The  $J = -1$  distribution from the LES is broader than for the experiment, as is reflected by the LES having

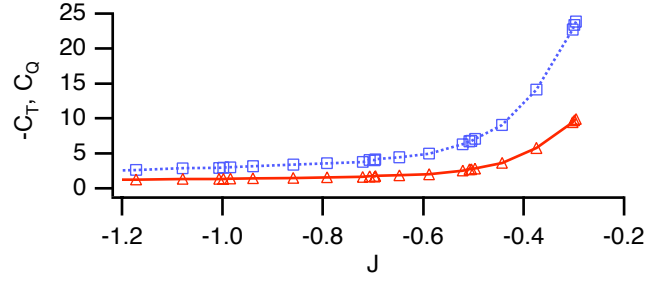


Figure 8. Mean propeller thrust and torque from VPWT<sup>8</sup> normalized by dynamic pressure.  $\triangle$  :  $C_T$  ;  $\square$  :  $C_Q$ .

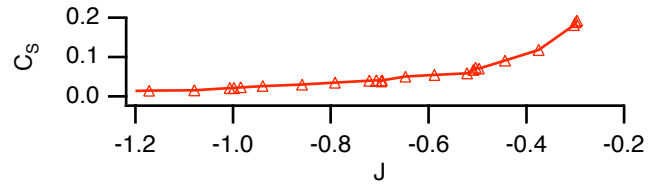


Figure 9. Mean propeller side force magnitude from variable pressure water tunnel (VPWT) results of Jessup et al.<sup>8</sup> normalized by dynamic pressure.

a larger standard deviation.

The PDFs for side force magnitude are shown in Figure 11. Since side force magnitude is a single-sided function due to it being a magnitude for double-sided variables (i.e.,  $F_y$  and  $F_z$ ), it would be expected to be log-normally distributed. The LES and VPWT distributions for  $J = -0.5$  match very closely. For  $J = -0.7$  the LES has a higher peak and narrower distribution than for the VPWT and for  $J = -1$  the LES and VPWT data have close to the same peak but the LES distribution decrease more slowly than the VPWT data for larger values of side force magnitude.

The skewness of a PDF is its tendency to favor one side of the mean. Figure 12(a), a plot of skewness as function of  $J$  for thrust shows that both LES and VPWT have slightly negative skewness remaining fairly constant with  $J$ . The skewness for side force magnitude, Figure 12(b) shows that it has positive skew that increases slightly as  $J$  becomes more negative.

Kurtosis is a measure of the “peakedness” of a PDF where higher values mean that more of the RMS is due to infrequent extreme deviations, as opposed to frequent moderately-sized deviations. Kurtosis is normalized so that a Gaussian distribution has a value of zero. Figure 13 shows that the VPWT kurtosis values are slightly greater than zero and increase as  $J$  becomes more negative. The LES values are close to the VPWT values but have an inconsistent trend with  $J$ .

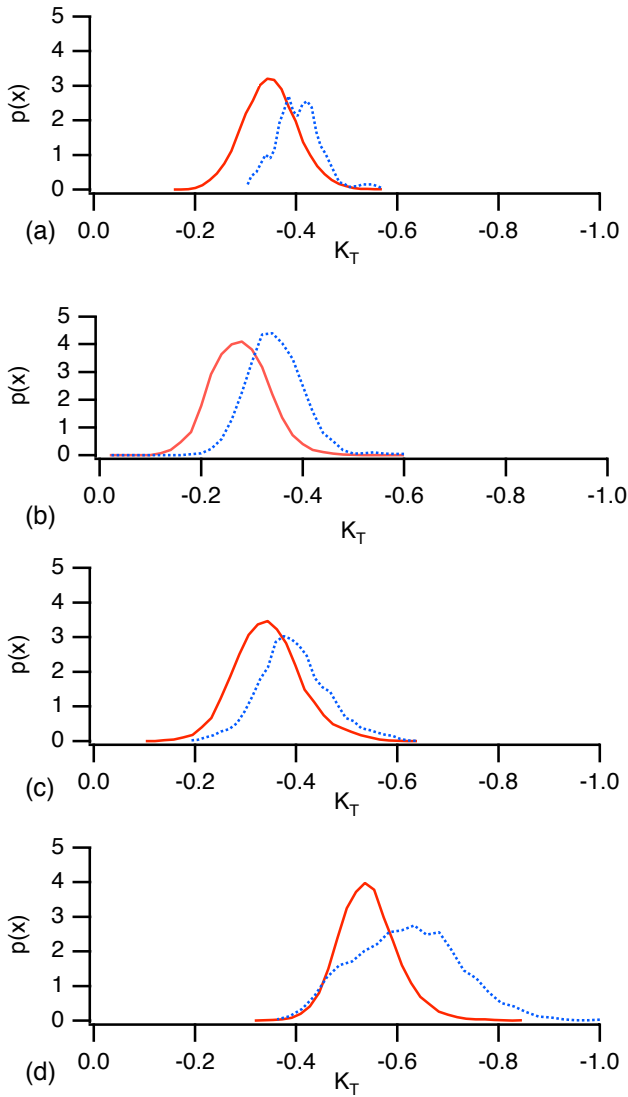


Figure 10. PDFs for  $K_T$  for (a)  $J = -0.3$ , (b)  $J = -0.5$ , (c)  $J = -0.7$ , and (d)  $J = -1.0$ ; VPWT experiments: — ; LES: ····· .

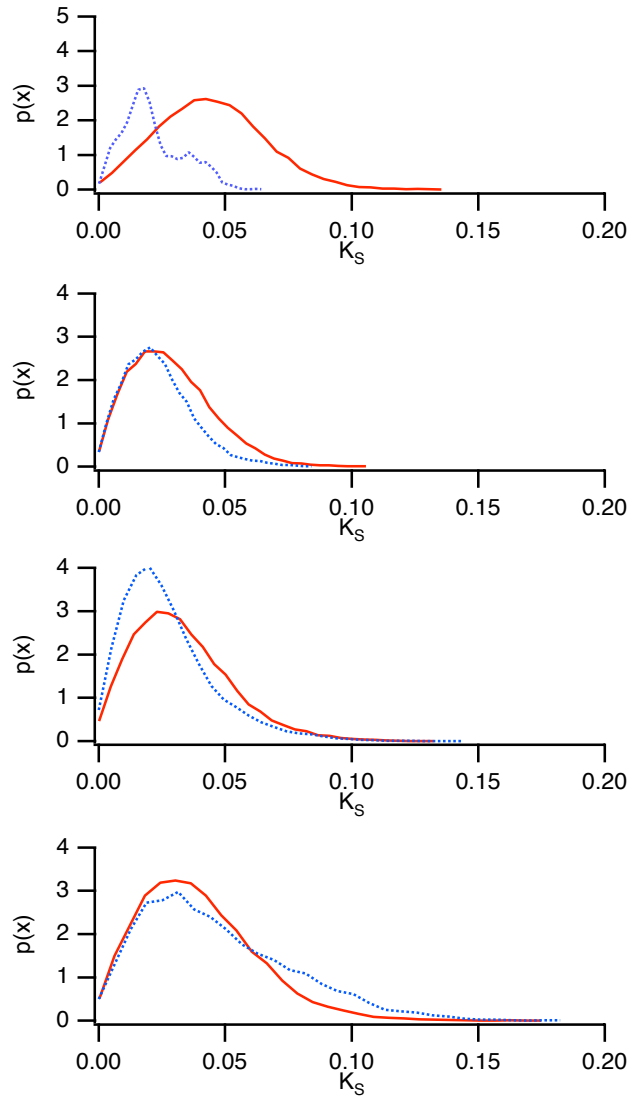


Figure 11. PDFs for  $K_S$  for (a)  $J = -0.3$ , (b)  $J = -0.5$ , (c)  $J = -0.7$ , and (d)  $J = -1.0$ ; VPWT experiments: — ; LES: ····· .

### 3.3 Power Spectral Densities

Figure 14 shows the PSD of side force magnitude for the VPWT experiments and the simulations for the four LES  $J$  values. The PSD were computed by dividing the force time histories into  $N$  segments with 50% overlap, applying a Hanning window to minimize end effects, rescaling to maintain the original energy, taking the Fourier transform of the segment, computing the square of the magnitude of the complex Fourier transform and then dividing by the frequency resolution. The PSD computed for each of the segments were then averaged. The segment lengths were selected so as to be long enough to obtain a

frequency resolution small enough to characterize possible low frequency events yet provide enough segments for a relatively smooth curve. The sum of the magnitudes for a one-sided spectra equals the mean square of the original signal. The abscissa of the PSD plots is the frequency normalized by the shaft frequency (11.667 Hz) and therefore, has the units of Hz/revolution.

Thangam, Wang and Zhou<sup>22</sup> explain that in the inertial frequency range of the turbulent kinetic energy (TKE) spectrum, for flows with high rotation rates, there exist two, rather than one, time scales: the eddy turnover time scale *and* the time scale associated with the rotation rate. The Kolmogorov spectrum, instead

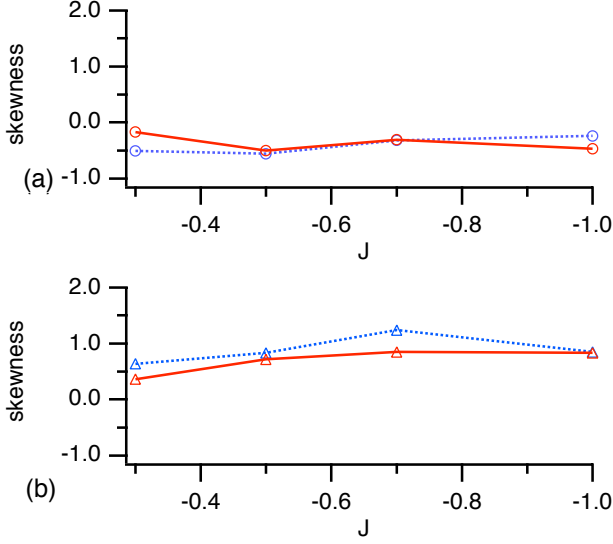


Figure 12. Skewness for (a)  $K_T$  and (b)  $K_S$ ; VPWT experiments: — ; LES: .....

of behaving as  $f^{-5/3}$ , rolls off as  $f^{-2}$ . Assuming pressure to be proportional to TKE we can expect the same behavior. This can be clearly seen in the VPWT and LES PSD where for  $J = -0.3$  and  $J = -0.5$  the PSD exhibits a  $f^{-2}$  behavior down to almost  $f^* = 1$ . for  $J = -0.7$  and  $J = -1$  the slope is less —  $f^{-5/3}$  — as  $J$  becomes more negative. This is not surprising since as  $J$  becomes more negative,  $U$  increases with constant  $n$ , and the effect of rotation becomes less significant.

In the experimental PSD a peak at shaft rate ( $f^* = 1$ ) is caused by small force oscillations due to not being able to exactly account for the weight of the propeller while the load dynamometer rotates about the shaft. This peak is not in the LES PSD. Most noticeable is a peak at blade rate ( $f^* = 5$ ) which may be due to the passage of blades through flow disturbances fixed in the inertial frame of reference — a fixed disturbance would be encountered five times per shaft revolution. The relative height of the blade rate peak decreases as  $J$  becomes more negative, indicating that multi-scales of turbulence become more important as  $J$  decreases. A wider peak appears at twice the blade rate,  $f^* = 10 - 15$ . Its importance diminishes as  $J$  becomes more negative.

The VPWT and LES data compare well in the low-frequency range ( $f^* < 1$ ), with the exception of  $J = -0.3$ , which is consistently low. The peak value at blade rate is well-predicted by the LES at all  $J$  although the energy around the peak is increasingly well-predicted as  $J$  becomes more negative. The twice blade rate peak shows up in the lower negative  $J$  cases, but disappears completely for the higher negative  $J$  cases. This may be

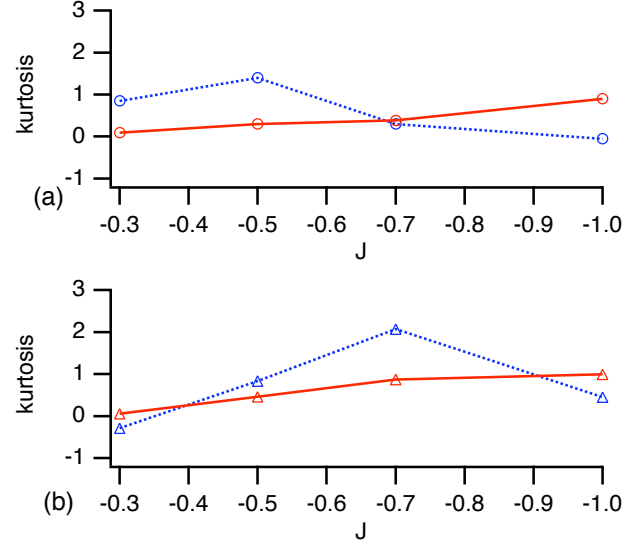


Figure 13. Kurtosis for (a)  $K_T$  and (b)  $K_S$ ; VPWT experiments: — ; LES: .....

due to the computational grid's decreasing ability to resolve the viscous turbulence scales on the blades as Reynolds number increases as  $J$  becomes more negative. The frequency equivalent to the computational time step size is 1680 times the shaft rate for the LES, so the discrepancies in the PSD at twice blade rate is not due to temporal resolution. Therefore, these discrepancies may be due to factors such as wall normal grid spacing on the blades. Particularly where the flow on the blade surfaces is not separated, finer wall-normal resolution in the near wall region would enhance the initiation of near-wall turbulence structures which may contribute to the higher frequency loading.

Jiang et al.,<sup>10</sup> in experiments performed at  $J = -0.472$  and  $J = -0.732$ , observed that HA events occur at  $\omega D/U = 0.5$ . For  $J = -0.5$  this implies a low-frequency peak at  $f^* = 0.040$  which can be seen in the PSD as the second frequency bin. Longer time series, which result in better frequency resolution, are needed to fully evaluate this behavior.

### 3.4 Blade loading

The ultimate objective of this project to accurately predict blade strains and deformations during crashback. Jessup et al.<sup>9</sup> measured blade surface strains near the blade root during VPWT experiments. It is possible to compare with their results if it is assumed that strain is proportional to stress which in turn is proportional to bending moment (BM). In order to compute BM, a single blade has been divided into 12 constant-radius sections from which the forces due to pressure are computed. The BM due to these 12 strips is computed about the axis perpendicular

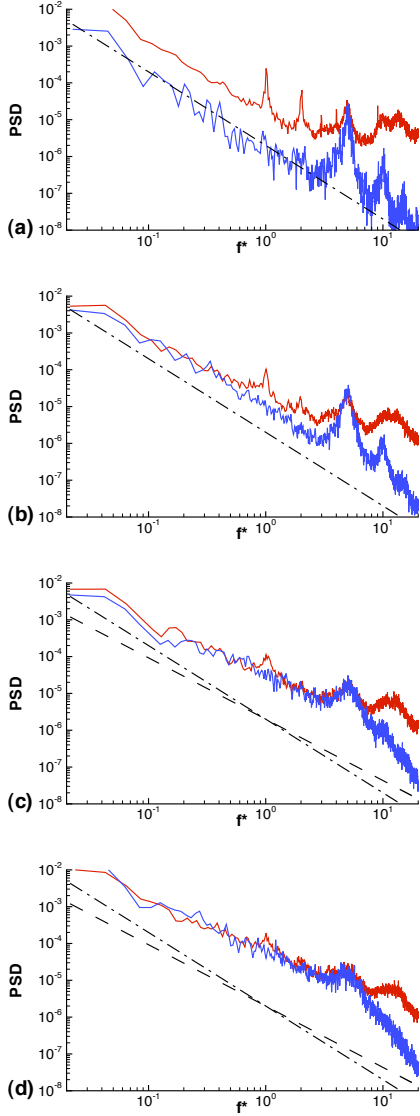


Figure 14. Side force magnitude PSD for (a)  $J = -0.3$  (b)  $J = -0.5$  (c)  $J = -0.7$  and (d)  $J = -1.0$  blue: LES, red: VPWT experiment,  $-\cdot-$  :  $f^{-2}$  roll off and  $- - -$  :  $f^{-5/3}$  roll off.

to the strain gauge measurement direction. Figure 15 is a composite image showing the pressure coefficient on the blades, the thrust ( $K_T$ ) at each section and the thrust for the entire blade for  $J = -0.5$  during a HA loading event. The pressure coefficient is defined by

$$C_p = \frac{p}{\frac{1}{2}\rho U^2} \quad (15)$$

In the upper part of Figure 15 the leading edge of the suction side is the left side of the blade. A very low pressure region can be seen on the leading edge near the tip which generates the tip-loaded thrust profile in the lower right image of Figure 15. Figure 16 is a HA loading example for  $J = -1$ . In contrast to the loading for  $J = -0.5$ , the section thrust distribution is much smoother, peaking near  $r/R = 0.7$ .

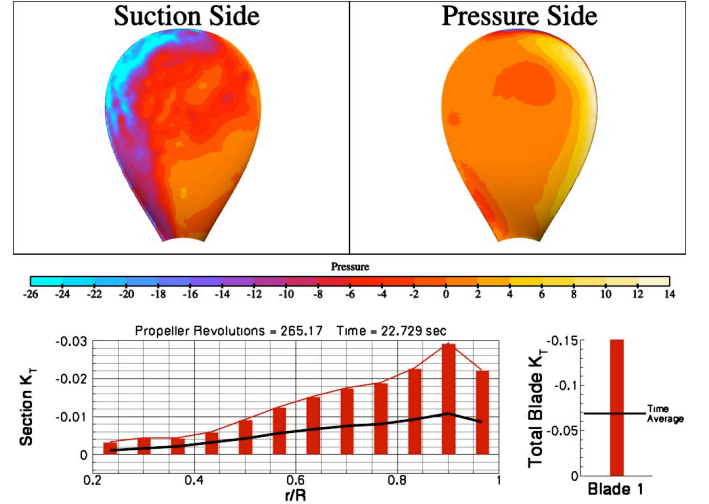


Figure 15. HA blade loading example for  $J = -0.5$ . Upper: pressure ( $C_p$ ) contour plots on suction (aft face) and pressure (forward face) sides of blade; lower left: spanwise distribution of sectional  $K_T$  with temporal mean reference line; lower right: total  $K_T$  for single blade with temporal mean reference line.

Figure 17 is a plot of the temporal mean of the spanwise thrust distribution for a single blade for  $J = -0.5$  and  $J = -1$ .  $J = -1$  has more of the traditional elliptical loading with a peak near  $r/R = 0.7$ .  $J = -0.5$ , on the other hand, increases almost linearly from the root out to its peak at  $r/R = 0.9$  reflecting the tip-loaded behavior in Figure 15.

In order to ascertain whether the LES can accurately predict the HA strains, the ratios of the maximum  $\mathcal{M}$ ,  $\mathcal{M} + 2\sigma$ ,  $\mathcal{M} + 3\sigma$  normalized by the mean BM have been computed.  $\mathcal{M}$  denotes bending moment and  $\sigma$  denotes the standard deviation of the BM. Figure 18 compares the BM ratios from the LES to the same strain ratios from the VPWT experiments. The  $\mathcal{M} + 2\sigma$   $\mathcal{M} + 3\sigma$  curves have peaks at  $J = -0.5$  and the maximum  $\mathcal{M}$  has a peak at  $J = -0.65$ . The LES data compare very well with the experiments at  $J = -0.5$  and  $J = -1$ . This is an indication of the accuracy of the HA force function data which will be used in finite element analyses.

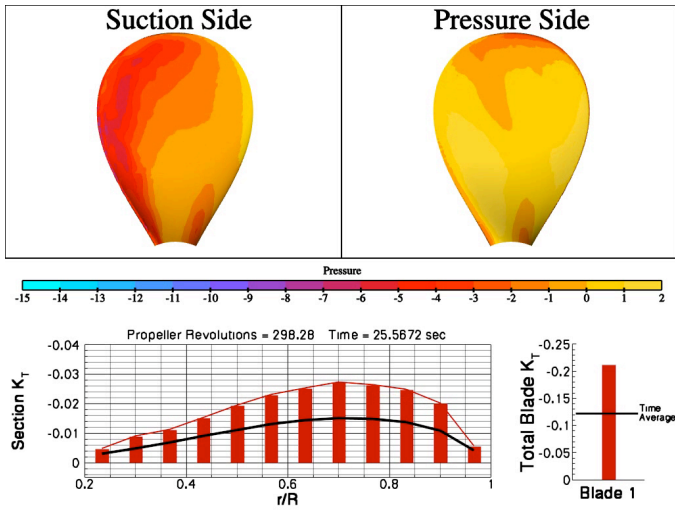


Figure 16. HA blade loading example for  $J = -1$ . Upper: pressure ( $C_p$ ) contour plots on suction (aft face) and pressure (forward face) sides of blade; lower left: spanwise distribution of sectional  $K_T$  with temporal mean reference line; lower right: total  $K_T$  for single blade with temporal mean reference line.

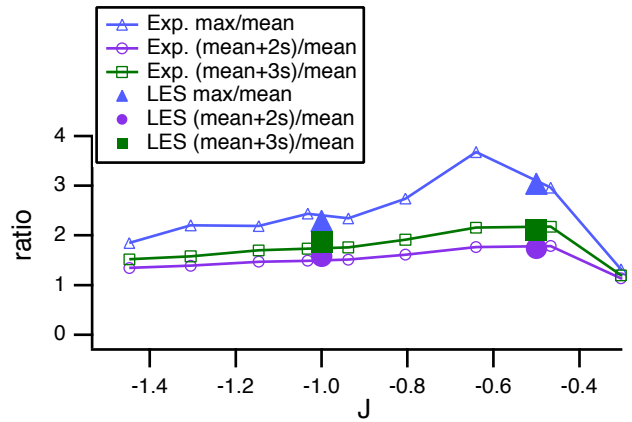


Figure 18. Bending moments from LES compared with strains from experiment.  $\circ$ :  $\tau + \sigma$ ;  $\square$ :  $\tau + 2\sigma$ ;  $\triangle$ :  $\tau_{max}$ ; Solid symbols: LES.

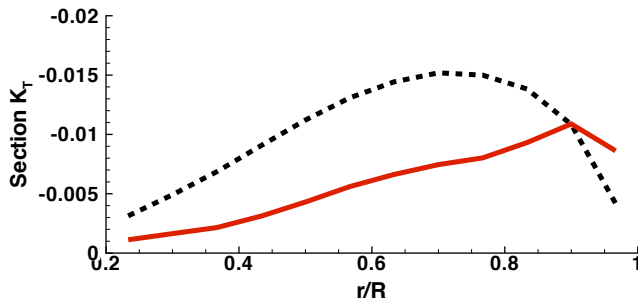


Figure 17. Time average loading distribution for —:  $J = -0.5$  and ---:  $J = -1$ .

### 3.5 Physics of Crashback

In this section we investigate the physics of high- and low-amplitude loading to try to understand the causes of high thrust and side force magnitude. A physical understanding will aid in knowing the optimal computational methodologies to apply and knowing what data are needed for development of low-order predictive tools among other things. In each of the force time histories, comprising several hundred revolutions, several HA events stand out and are the cause of high structural loading and side forces. For  $J = -0.5$  we look at a HA event at  $t^* = 265$  and compare to a very low-amplitude (LA) event at  $t^* = 140$ , where  $t^* = tn$  is time normalized by the time per revolution. For  $J = -1$  we look at a HA event found at  $t^* = 300$  and compare it with a LA event at  $t^* = 290$ . The surface pressures from these events have been used as the input loads for dynamic structural analyses which are documented in the following section.

How representative these events are of “typical” events can be answered by assessing where the events are on the PDFs or how many SD they are from the mean: For  $J = -0.5$  the maximum  $K_T$  during the selected HA event is  $K_T = -0.61$  which is  $4.9\sigma$  less than the mean and at the far right side of the PDF, Figure 10(b) meaning that it is an extreme event. The LA event at  $t^* = 140$  has  $K_T = -0.141$  which is  $1.6\sigma$ . For  $J = -1$ ,  $t^* = 290$  is the LA loading event that we study, it has  $K_T = -0.525$  which is  $0.8\sigma$  greater than the mean, and therefore, is fairly common. For  $J = -1$  the HA loading event is at  $t^* = 300$  which has  $K_T = -0.833$  which is  $2.2\sigma$  less than the mean.

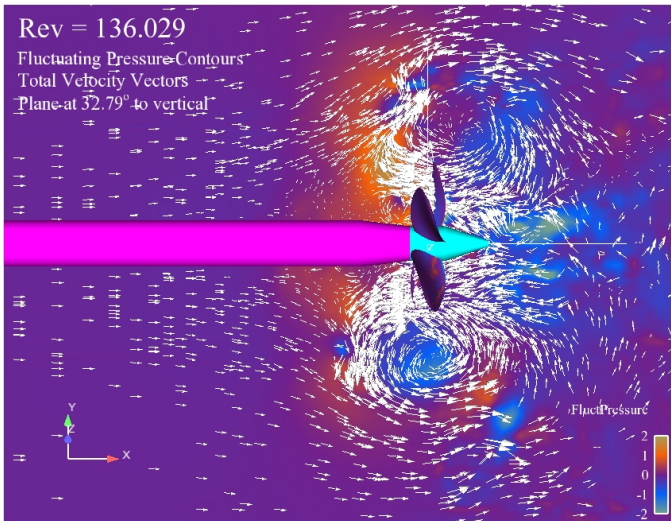


Figure 19. Lateral plane cut showing contours of fluctuating pressure and total velocity vectors showing typical VR mode behavior.

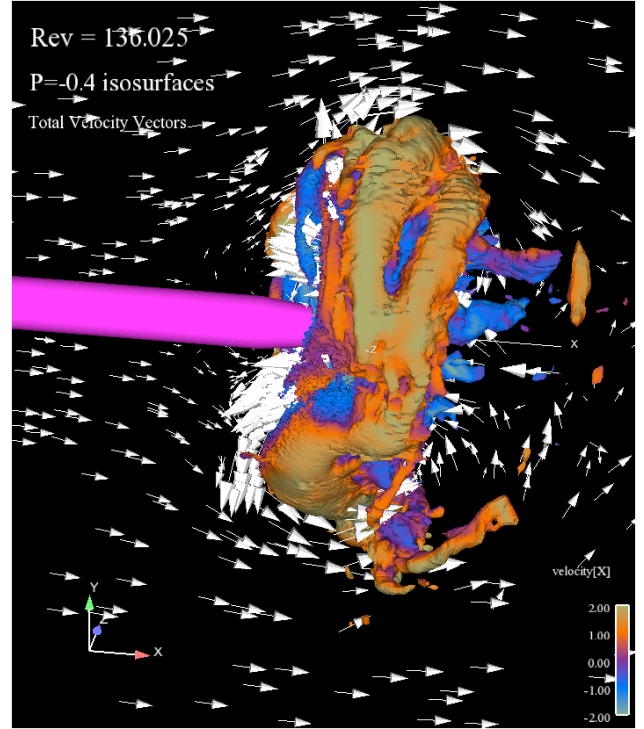


Figure 20. Iso-surfaces of  $C_p = -0.4$  colored by axial velocity and total velocity vectors showing typical VR mode behavior.

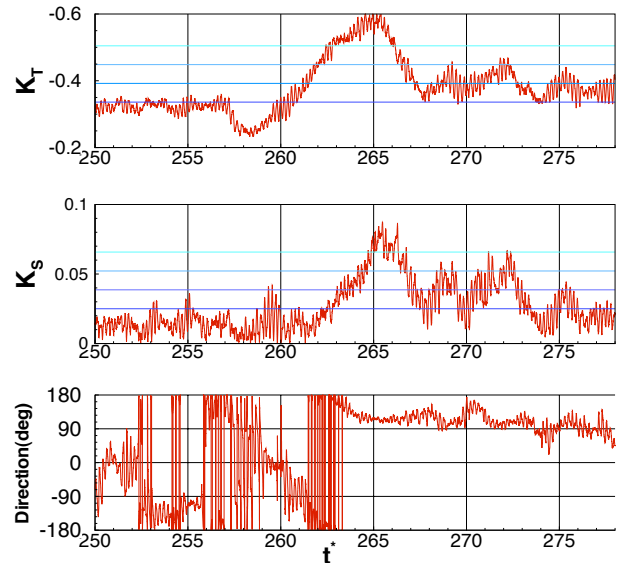


Figure 21. Force time history for  $J = -0.5$  HA event at  $t^* = 265$ . Top:  $K_T$ , middle:  $K_S$  and bottom: side force angle.

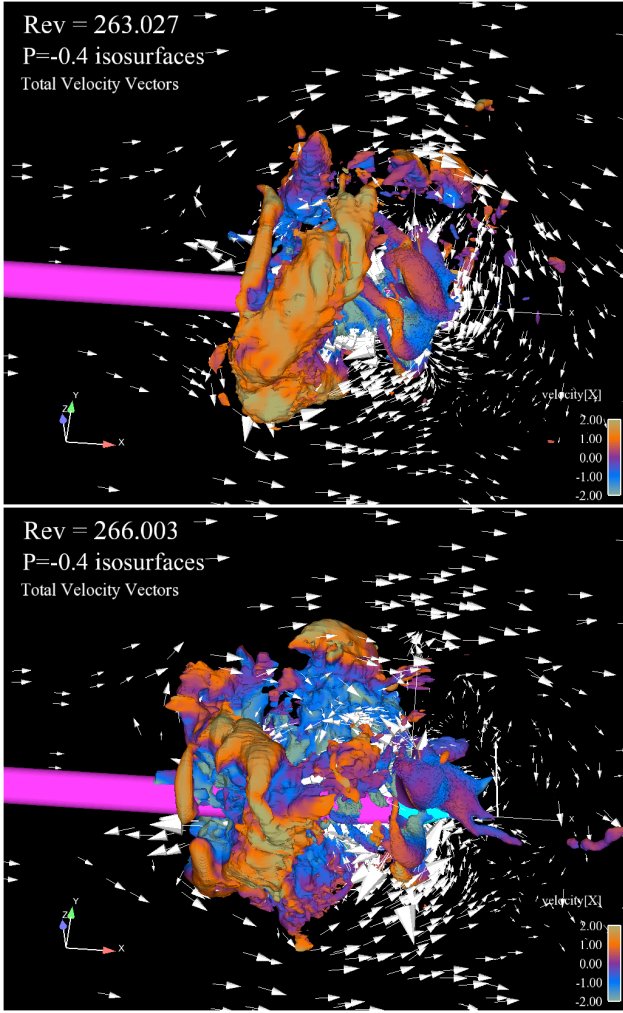


Figure 22. Iso-surfaces of  $C_p = -0.4$  colored by axial velocity and total velocity vectors showing upper: transition between VR to AJ modes and lower: AJ mode.

**3.5.1  $J = -0.5$  Low Amplitude Behavior** Figure 19 is a centerplane cut showing contours of fluctuating pressure and velocity vectors at a time close to  $t^* = 140$ . It shows a vortex ring (VR) centered axially about the blade centerplane and radially about  $0.5D$  outboard of the propeller tips that is circumferentially uniform with a uniform axial inflow into the propeller. Figure 20 are iso-surfaces of  $C_p = -0.4$  which show a symmetric RV structure. Figure 29(lower left) shows that the inflow into the propeller is relatively uniform with insignificant in-plane components. Iso-surfaces of  $\lambda_2$  are shown in Figure 29(right).  $\lambda_2$ , the second eigenvalue of the second invariant of the velocity gradient tensor, can differentiate between regions of high vorticity but no rotation (as in boundary layers) and regions of high vorticity and vortical motion (as in turbulence structures).<sup>7</sup> The  $\lambda_2$

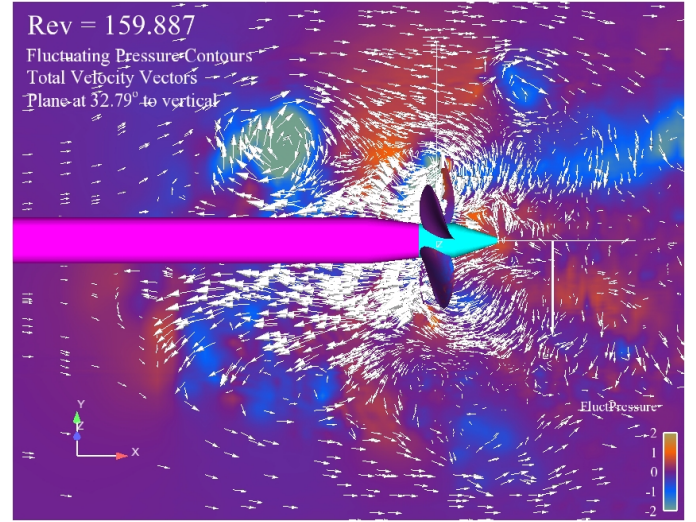


Figure 23. Lateral plane cut showing contours of fluctuating pressure and total velocity vectors showing typical AJ mode behavior.

iso-surfaces show that the blades have small amounts of leading edge separation and on Blade 1, a blob at about  $r/R = 0.4$ , is probably a separation vortex that has detached from the leading edge. On all blades  $\lambda_2$  tip vortices are being shed.

The effect of the turbulence structures on the side force is demonstrated in Figure 29(upper left) which shows the aft blade faces colored by pressure force parallel to the side force vector at each point on the blade surface,  $f_{ps}$  (labeled as “pfyp” in the plots), is defined as:

$$f_{ps} = C_p |d\mathbf{A}| \frac{d\mathbf{A}}{|d\mathbf{A}|} \cdot \frac{\mathbf{F}_s}{|\mathbf{F}_s|} \quad (16)$$

where  $d\mathbf{A}$  is the differential area vector and  $\mathbf{F}_s$  is the resultant side force vector. The contours, then, indicate where on the blades the side force is generated. In orange-colored regions the pressure is acting in the direction of the side force vector, whereas the blue regions act in the opposite direction. The visible regions coincide with the turbulence structures in Figure 29(right).

**3.5.2  $J = -0.5$  High Amplitude Behavior** In Figure 21 at about  $t^* = 260$  the loading begins to increase. In conjunction with this increase the VR transforms into an axial jet as shown in the pressure iso-surfaces Figure 22(top), where in the upper image the VR is translating forward, though still maintaining a tilted, ring-like structure. It reaches a AJ state, Figure 22(bottom) where the ring has been stretched forward beyond recognition. Figure 23 is a plot of fluctuating pressure contours

and velocity vectors on a center plane for a typical AJ event. The flow is dominated by an axial jet along the shaft that extends three  $D_p$  upstream of the propeller plane. The return flow outboard of the jet is weak providing reduced axial flow aft of the propeller.

Figure 30(right) shows contours  $\lambda_2 = -4$  colored by axial velocity. Here blue represents velocity in the upstream direction and orange, flow downstream. The blade surfaces are the source of turbulence structures, particularly at the leading edges, where structures are present along their length, with shedding at the tip. There are also larger blob-like structures further along the chord that could be large separation vortices. These appear to coincide with the regions of side force generation shown in Figure 30(upper left). Side forces are generated only where the surface normal has a component in the plane of the propeller. The surface normal at the blade tips is primarily in the axial direction, whereas it has a much larger component in the propeller plane near the root due to blade twist. Therefore, side force is particularly sensitive to low pressure regions near the root. Blade 2 appears to be generating most of the side force with contributions from 1, 3 and 5. These side force generation regions coincide with large separation vortices in Figure 30(right).

Figure 30(lower left) shows the total axial velocity contours and the in-plane vectors directly aft of the propeller plane. The vectors show that the flow is primarily in the positive  $z$  direction. Thus, the blades that are rotating about the positive  $x$  direction will be heading directly into the oncoming flow leading to high AOA and flow separations. Jessup et al.<sup>8</sup> hypothesized that the side force should be in the same direction as the mean in-plane flow.

The HA side force events tend to have a duration on the order of 10 revolutions during which time the side force angle remains relatively constant. This means that the macro flow must remain in a relatively stable configuration. It is hypothesized that when the angle of attack on the blades increases, the blade imparts greater thrust and momentum to the fluid at that azimuthal (angle about the shaft centerline) location and at the same time creates a low pressure region. The low pressure region tends to draw fluid toward it maintaining the in-plane flow contrary to the propeller rotation. At the same time, the increased axial momentum in the upstream direction enhances the AJ flow along the upstream shaft. The downstream-directed return flow is weakened which in turn weakens the VR. Without the VR the axial flow upstream into the propeller is reduced, which again increases the angle of attack on the blades, increasing the thrust, thus self-perpetuating the process.

**3.5.3  $J = -1$  Low Amplitude Behavior** Figure 24 is a partial time history around the  $t^* = 290$  and  $t^* = 300$  low- and high-amplitude loading events that will be studied in detail. We examine the behavior at  $t^* = 290$  to get an idea of the flow when the thrust and side force magnitude are small. In Figure 25, a lat-

eral centerline cut, the flow is fairly symmetric about the centerline and the axial inflow is strong and relatively uniform. Figure 31(bottom left) verifies, in fact, the uniformity of the axial flow and the lack of in-plane velocities. The  $\lambda_2$  iso-surfaces in Figure 31(right) show little evidence of leading edge flow separations. The resulting side force magnitude is small, but not insignificant as shown in Figure 31(upper left). The pressure iso-surfaces in Figure 28 exhibit a symmetric morphology. It can be concluded that low loading is associated with symmetry.

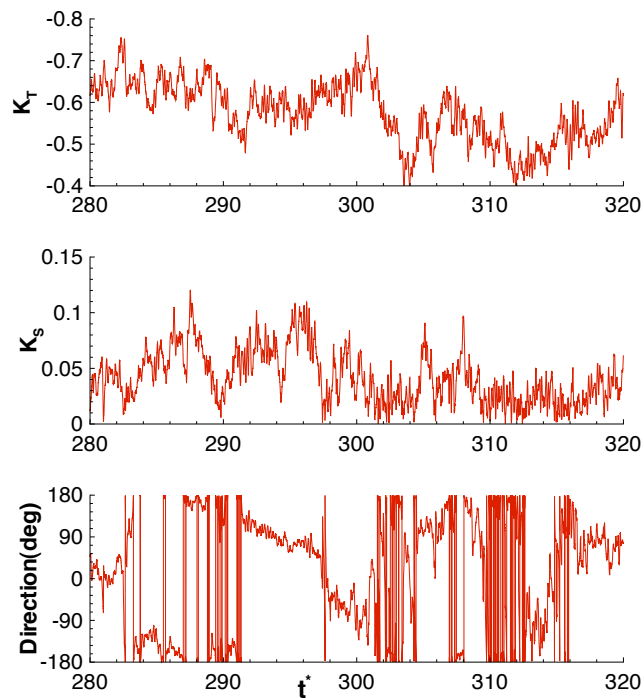


Figure 24. Force time history for  $J = -1$  HA event at  $t^* = 300$ . Top:  $K_T$ , middle:  $K_S$  and bottom: side force angle.

**3.5.4  $J = -1$  High Amplitude Event** In Figure 26, it is possible to see that the uniform axial inflow, characteristic of the LA loading, is no longer present. In fact, it appears that the upper portion of the RV has become detached and the axial flow into the upper portion of the propeller disk has been shifted upward. This allows a downstream incursion of fluid near the root, as seen in Figure 27. Figure 32(lower left), contours of axial velocity, show these incursions. Downstream-directed fluid would result in very high AOA and massive separation on the blades. Figure 32(right), iso-surfaces of  $\lambda_2$ , shows that on blades marked 2, 3 and 4, there is evidence of significant flow separa-

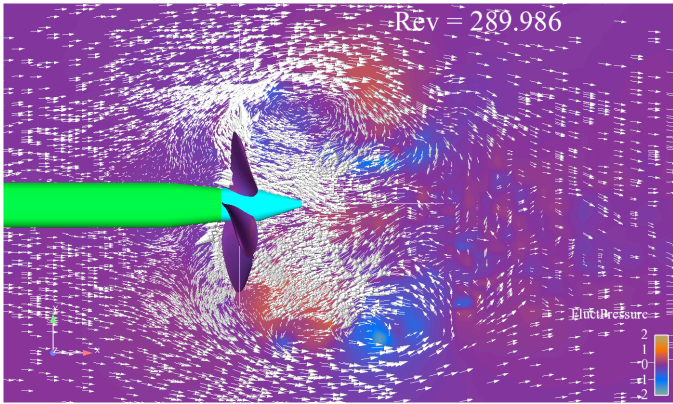


Figure 25. Lateral plane cut for  $J = -1$  at  $t^* = 290$  showing contours of fluctuating pressure and total velocity vectors during LA event.

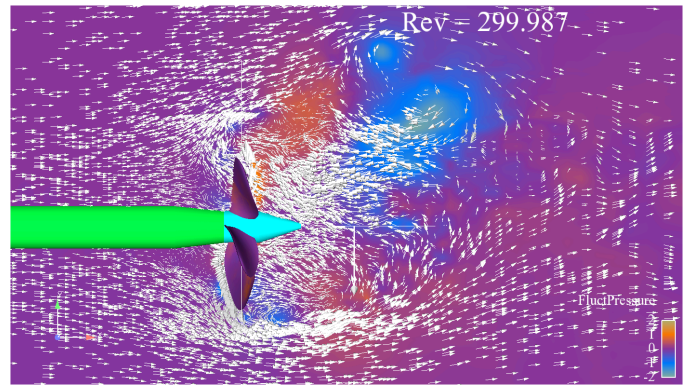


Figure 26. Lateral plane cut for  $J = -1$  at  $t^* = 300$  showing contours of fluctuating pressure and total velocity vectors for HA event.

tion near the root. This translates into side force since near the root as the surface normal is primarily in the side force direction, as shown in Figure 32(upper left). Animations of pressure iso-surfaces show that during the period  $296 < t^* < 300$  the RV goes through many complex morphologies including shedding, regeneration and stretching including deformation from a ring to an axial orientation whereby it gets wrapped around the propeller hub.

Understanding the flow at  $J = -1$  may shed some light on why the side force magnitude is so much higher for OW than it is for VPWT as shown in Figure 7. As seen for  $J = -1$  uniform streamwise inflow is a precondition for low side force. It is only when the flow is non-uniform that side force magnitude becomes significant. Moreover, it is the axial incursions of downstream flow which cause significant flow separation near the root, right where it can exert the most side force. In the OW experiments the propeller is mounted on a shaft is *behind* the propeller. This has the effect of strengthening the downstream inflow, since it does not have to flow over a shaft as in the VPWT experiments. The downstream shaft will affect the recirculation zone that forms behind the propeller, retarding the axial flow forward into the propeller. These two factors will each increase the likelihood of incursions of downstream flow at the root, thus exacerbating the flow separations. As  $J$  decreases for  $J < 0.6$  the inflow becomes stronger and the incursions stronger and more frequent, leading to an increase in side force magnitude. At higher  $J$  values ( $J > -0.6$ ) the thrust imparted on the fluid, as shown in Figure 8, is strong enough to overwhelm the downstream inflow, with RV moving forward, even with and ahead of the propeller plane such that any interactions with the downstream shaft would not have any affect on the side force magnitude.

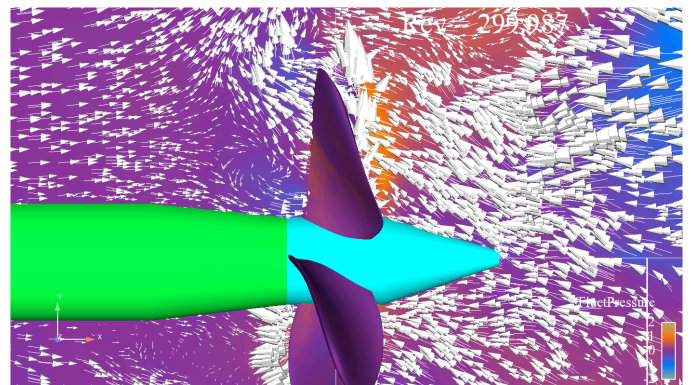


Figure 27. Flow at the root for  $J = -1$  at  $t^* = 300$  showing contours of fluctuating pressure and total velocity vectors for HA event.

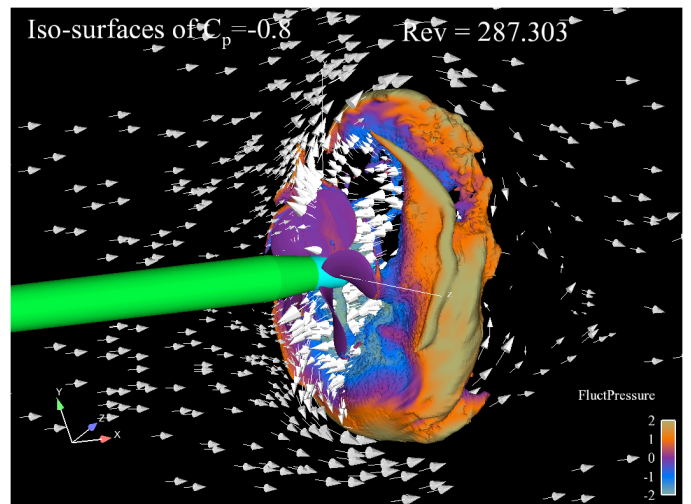


Figure 28. Iso-surfaces of  $C_p = -0.8$  for  $J = -1$  at  $t^* = 290$  during LA event.

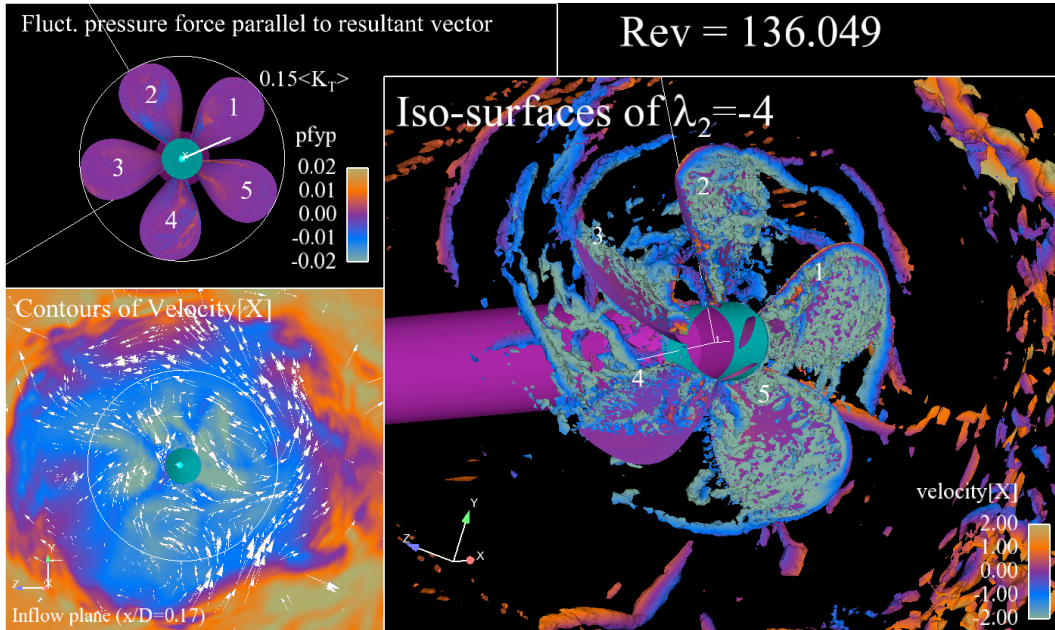


Figure 29. Composite graphic showing  $J = -0.5$  LA event at  $t^* = 136$ . Lower right:  $\lambda_2 = -4$  iso-surfaces colored by axial velocity; lower left: constant- $x$  cut at  $x/D = 0.167$  showing contours of axial velocity and velocity vectors; upper left: side force vector and aft blade surfaces showing contours of pressure force parallel to resultant side force vector.

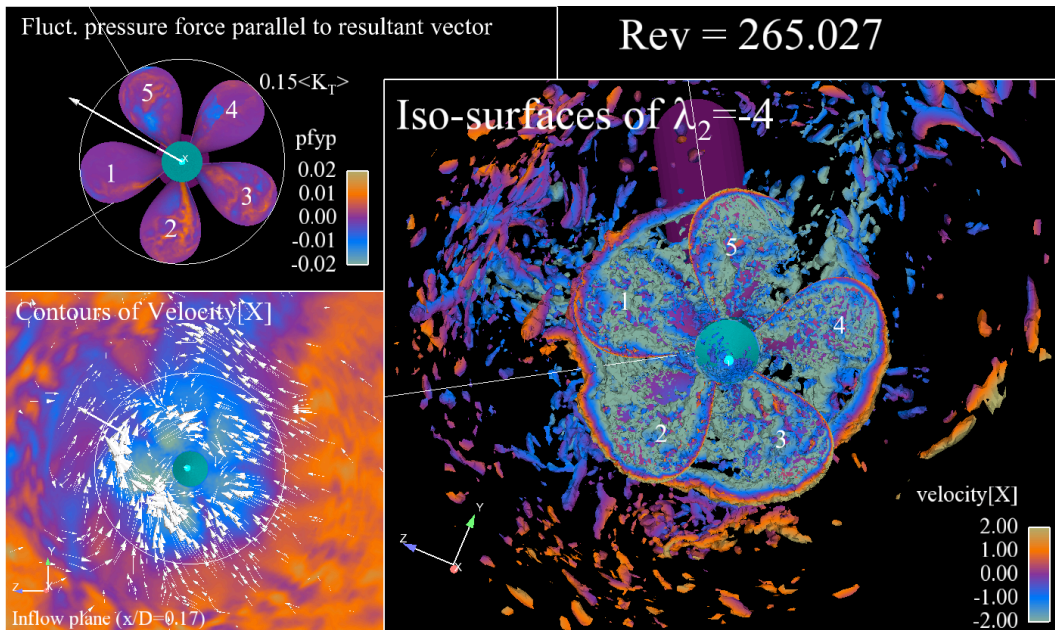


Figure 30. Composite graphic showing  $J = -0.5$  LA event at  $t^* = 265$ . Lower right:  $\lambda_2 = -4$  iso-surfaces colored by axial velocity; lower left: constant- $x$  cut at  $x/D = 0.167$  showing contours of axial velocity and velocity vectors; upper left: side force vector and aft blade surfaces showing contours of pressure force parallel to resultant side force vector.

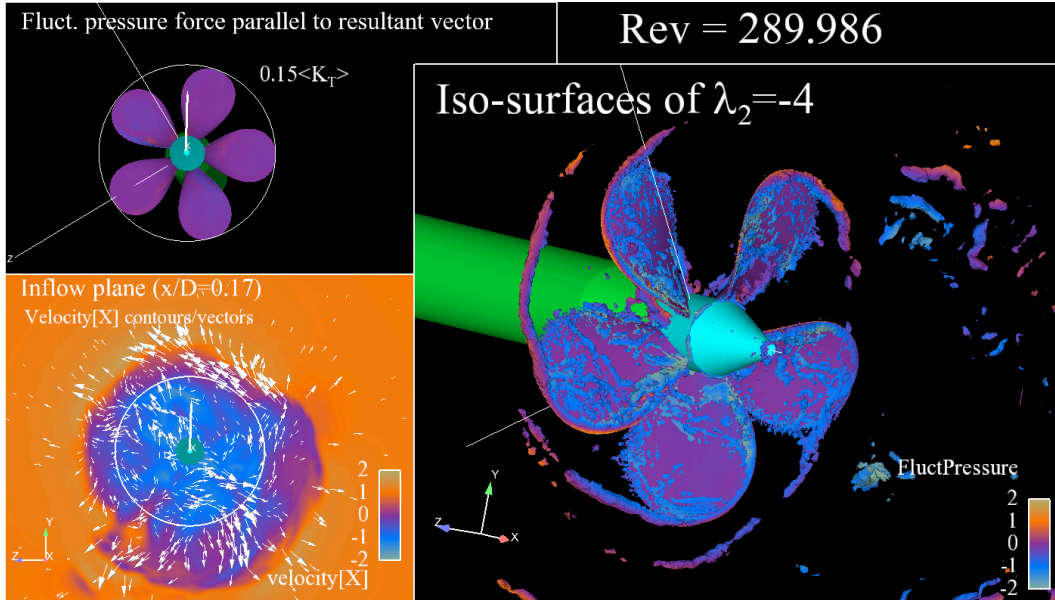


Figure 31. Composite graphic showing  $J = -1$  LA event at  $t^* = 290$ . Lower right:  $\lambda_2 = -4$  iso-surfaces colored by axial velocity; lower left: constant-x cut at  $x/D = 0.167$  showing contours of axial velocity and velocity vectors; upper left: side force vector and aft blade surfaces showing contours of pressure force parallel to resultant side force vector.

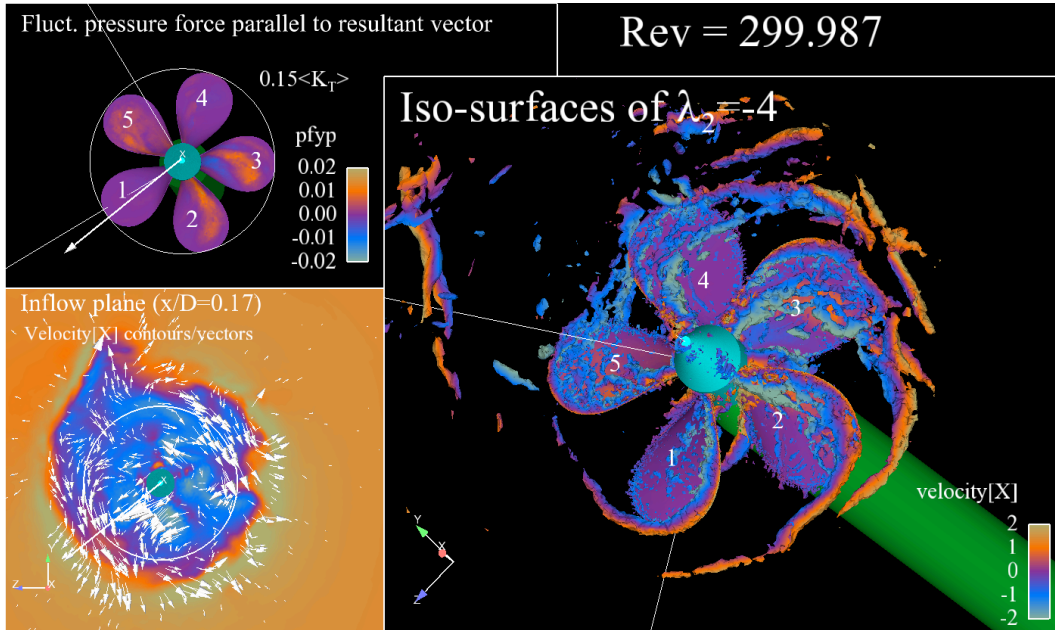


Figure 32. Composite graphic showing  $J = -1$  HA event at  $t^* = 300$ . Lower right:  $\lambda_2 = -4$  iso-surfaces colored by axial velocity; lower left: constant-x cut at  $x/D = 0.167$  showing contours of axial velocity and velocity vectors; upper left: side force vector and aft blade surfaces showing contours of pressure force parallel to resultant side force vector.

### 3.6 Dynamic Structural Response during Crashback

Based on the thrust force time histories from the LES simulation, four revolutions were chosen as representative cases that characterize the various hydrodynamic modes. They are respectively  $t^* = 140$  and  $t^* = 265$  for  $J = -0.5$ , and  $t^* = 290$  and  $t^* = 300$  for  $J = -1.0$ , where  $t^*$  is the simulated revolution number. For instance,  $t^* = 140$  means the pressure fields for  $140 < t^* < 141$  are applied to obtain the transient structural response.

In order to evaluate the structural integrity of the propeller subject to crashback, the dynamic response of the 0.3048 m diameter model-scale propeller 4381 made of aluminum (6061 T6) was investigated. The material has a Young's modulus of  $E_s = 73 \text{ GPa}$ , Poisson's ratio of  $\nu_s = 0.33$ , density of  $\rho_s = 2700 \text{ kg/m}^3$ , and yield stress of  $\sigma_y = 400 \text{ MPa}$ . To evaluate the potential yielding behavior, the von Mises criterion is adopted. The von Mises stress is defined as  $\sigma^v \equiv \sqrt{0.5[(\sigma_1 - \sigma_2)^2 + (\sigma_2 - \sigma_3)^2 + (\sigma_3 - \sigma_1)^2]}$ , where  $\sigma_1$ ,  $\sigma_2$ , and  $\sigma_3$  are the principal stress components. Based on convergence studies, three layers of quadratic brick (C3D20) and triangular prism (C3D15) continuum solid elements<sup>1</sup>, stacked in the thickness direction, were used to discretize the blade. In the chord and radial directions, 25 and 20 elements are used respectively. The blade discretization is shown in Figure 33.

The computed in air (dry) and in water (wet) natural frequencies of the aluminum propeller are shown in Figure 34. It can be seen that added mass effect leads to significant reduction of the natural frequencies. However, the fundamental wet frequency of 468 Hz is still much higher than the primary blade rate turbulent flow excitation frequency, 58 Hz. Thus, resonance is not an issue for this problem.

The predicted structural responses for  $J = -0.5$  are shown from Figure 35 to Figure 39. The computed change in tip pitch angle and rake are shown in Figure 35, which confirms that the blade deformations, and hence fluid-structure interaction effects, are negligible for the model-scale aluminum propeller. A positive pitch angle deflection means that the pitch angle increases; a positive rake deformation is downstream. The blade deformations for the axial jet mode,  $t^* = 265$ , are in general much higher and less uniform over the flow cycle than that for vortex ring mode,  $t^* = 140$ . Similar patterns were observed for the maximum von Mises stress ( $\sigma_{max}^v$ ) comparisons shown in Figure 36. Nevertheless, the maximum stresses for both cases are still approximately an order of magnitude lower than the material yield stress of  $\sigma_y = 400 \text{ MPa}$ , indicating structural safety. Based on the von Mises stress contours as shown in Figure 37, the maximum stresses occur at the blade root near the mid-chord in general. The stress patterns are not symmetric due to loading and geometry non-uniformity. Notice that the stress levels for  $t^* = 265$  are much higher than those for  $t^* = 140$ . The stresses are predominantly bending, as shown in the bending stress contours (Figure 38), which closely resemble the von Mises con-

tours (Figure 37). The shear stress distributions are shown in Figure 39. Some localized high shear stress regions exist near the blade roots and blade leading edge. The high shear stress near the trailing edge is primarily caused by the sharp pressure gradient induced by the turbulent fluid as shown in Figure 15. The shear stress at the leading edge is shown in Figure 40.

For  $J = -1.0$ , the computed structural responses are shown from Figure 41 to Figure 45. Again, the fluid induced deformations are small enough to allow for decoupled structural analysis. As expected, the blade deformations and stresses are higher than those for  $J = -0.5$  due to the higher fluid loading. It is interesting to note that although only the vortex ring mode exists for this advance coefficient ( $J = -1.0$ ), significant differences can still be observed between the two representative revolutions, both in magnitude and variation pattern. In particular, five distinct peaks can be observed in the time histories of the blade deformations and maximum von Mises stresses for  $t^* = 300$ , which may cause the blades to be more susceptible to fatigue induced failure. For  $J = -1.0$ , the von Mises stress distributions are plotted in Figure 43. It can be seen that the stresses are higher than those for  $J = -0.5$  as shown in Figure 37. Moreover,  $t^* = 300$  features higher stress levels than  $t^* = 290$ . The same as for  $J = -0.5$ , the stress is primarily due to bending, as indicated by the similarity between the von Mises (Figure 43) and bending (Figure 44) stress patterns. Similarly, localized high shear stress regions can be found near the blade roots and blade leading edge as shown in Figure 45.

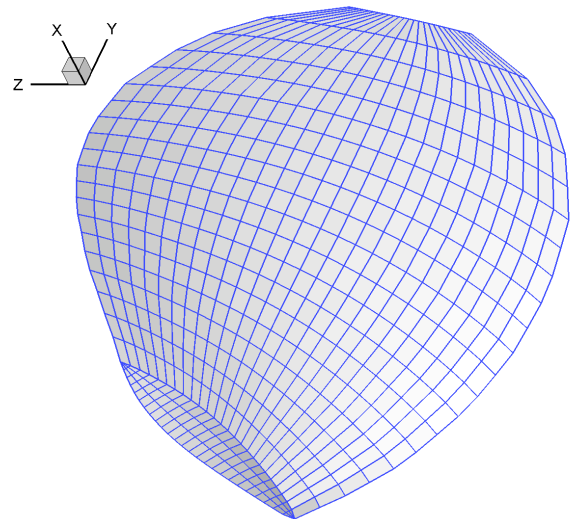


Figure 33. Mesh discretization of the key blade (a total of  $25 \times 20 \times 3 = 1500$  solid elements were used per blade).

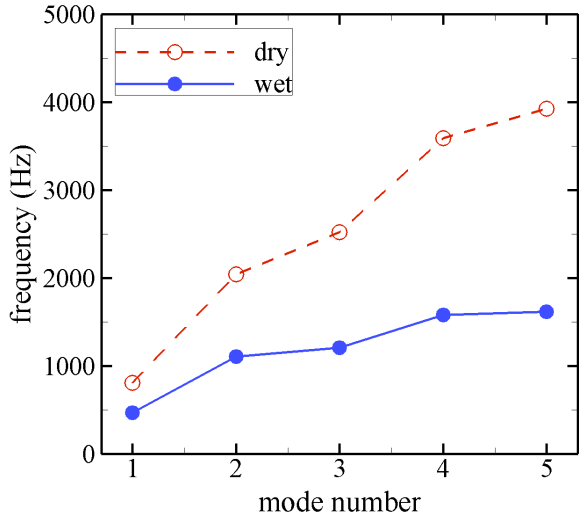


Figure 34. Predicted natural frequencies of the propeller 4381 (made of aluminum 6061 T6) in air (dry) and in water (wet).

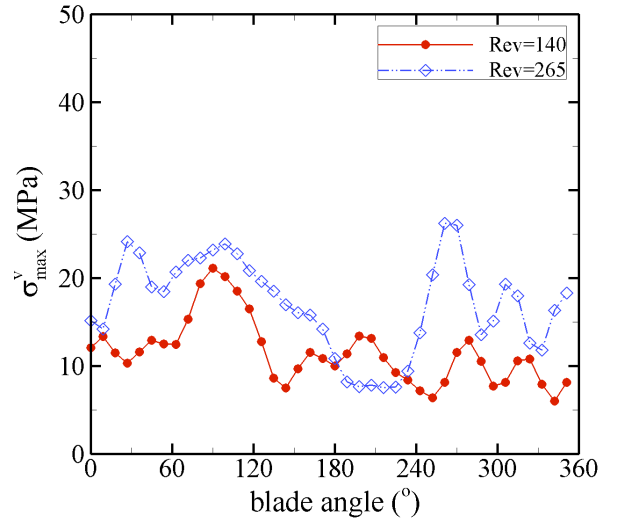


Figure 36. Predicted maximum von Mises stresses as a function of blade angles for  $t^*=140$  and  $t^*=265$  ( $J=-0.5$ ).

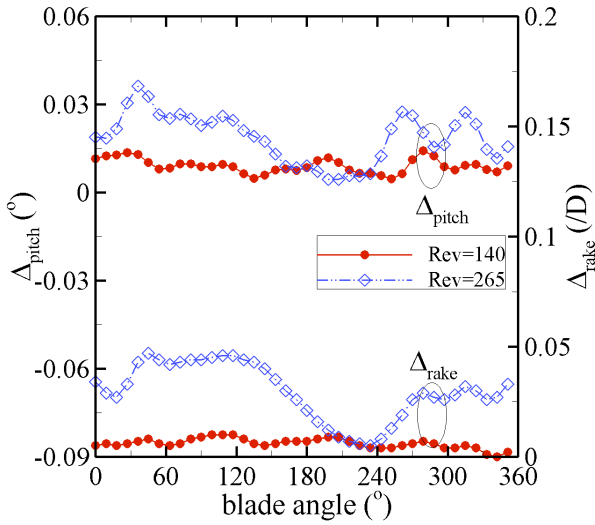


Figure 35. Predicted change in tip pitch angle and rake as a function of blade angles for  $t^*=140$  and  $t^*=265$  ( $J=-0.5$ ).

#### 4 CONCLUSIONS

This paper documents an extensive validation of a high-fidelity LES code's ability to predict crashback for a zero skew angle, model scale Propeller 4381. First order and higher order statistics, probability density functions, power spectral densities, and bending moment ratios have been compared with experimental data for a range of advance ratios ( $J$ ). The results demonstrate that the LES code is capable of simulating the turbulence scales necessary for accurate prediction of forces and moments during crashback and can be a viable design evaluation tool for predic-

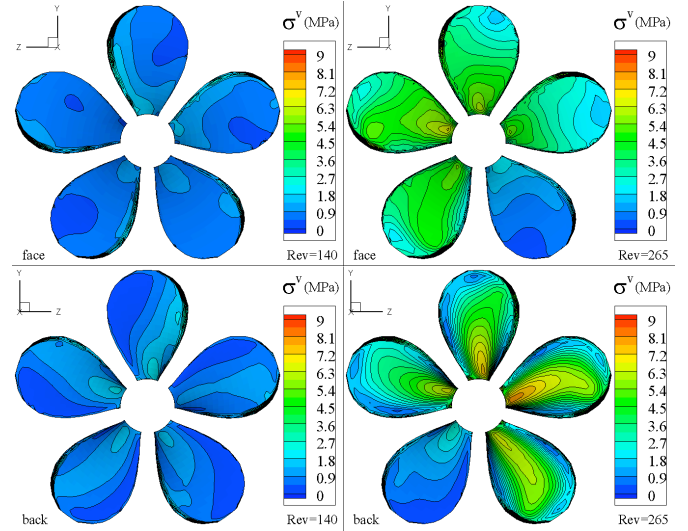


Figure 37. Predicted von Mises stress ( $\sigma^v$ ) contours at varying blade angles for  $t^*=140$  and  $t^*=265$  at  $J=-0.5$  (left-top: face side,  $t^*=140$ ; right-top: face side,  $t^*=265$ ; left-bottom: back side,  $t^*=140$ ; right-bottom: back side,  $t^*=265$ ).

tion of crashback loads.

The LES-generated database has been used to investigate the high- and low-loading events at two  $J$  values that have disparate physical processes. At low negative  $J$ , the propeller forces dominate the inflow and the flow has a bi-modal behavior switching between the familiar vortex ring (VR) mode and an axial jet (AJ) mode. During the AJ mode the magnitudes of the thrust and side forces are maximum. In other words, maximum decelera-

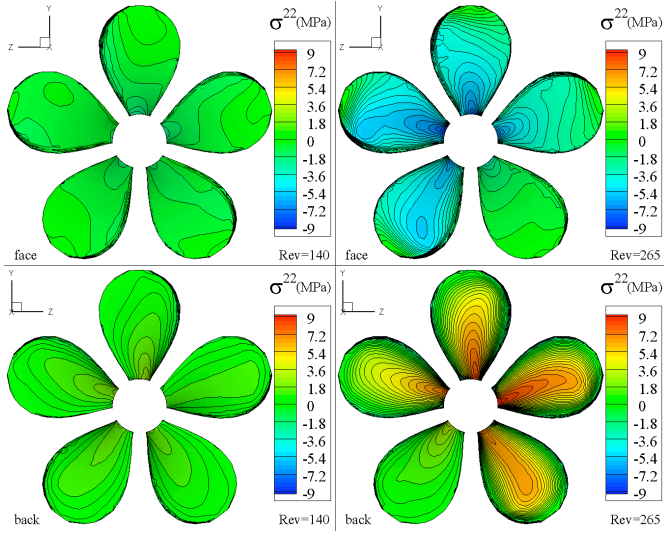


Figure 38. Predicted bending stress ( $\sigma^{22}$ ) contours at varying blade angles for  $t^*=140$  and  $t^*=265$  at  $J=-0.5$  (left-top: face side,  $t^*=140$ ; right-top: face side,  $t^*=265$ ; left-bottom: back side,  $t^*=140$ ; right-bottom: back side,  $t^*=265$ ).

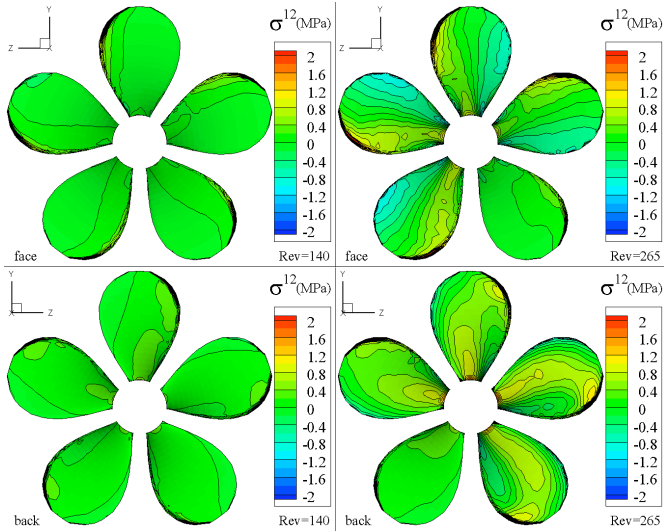


Figure 39. Predicted shear stress ( $\sigma^{12}$ ) contours at varying blade angles for  $t^*=140$  and  $t^*=265$  at  $J=-0.5$  (left-top: face side,  $t^*=140$ ; right-top: face side,  $t^*=265$ ; left-bottom: back side,  $t^*=140$ ; right-bottom: back side,  $t^*=265$ ).

tion is associated with maximum blade loading and side forces. At lower  $J$  values where the propeller thrust is of the order two times that of the incoming flow, VR asymmetries account for high loadings. In particular we have found that reverse (downstream) flow at the root is very effective at generating high levels of side force. Low loading events are associated with VR sym-

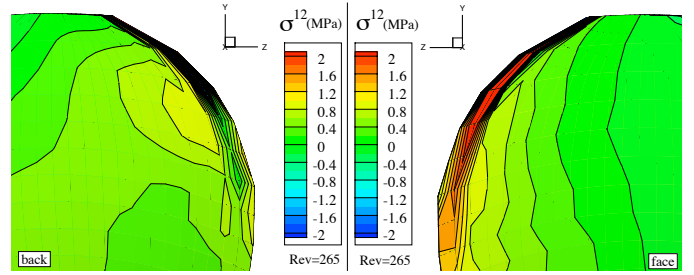


Figure 40. Predicted shear stress ( $\sigma^{12}$ ) contours  $t^*=265$  at  $J=-0.5$  (left: back side; right: face side).

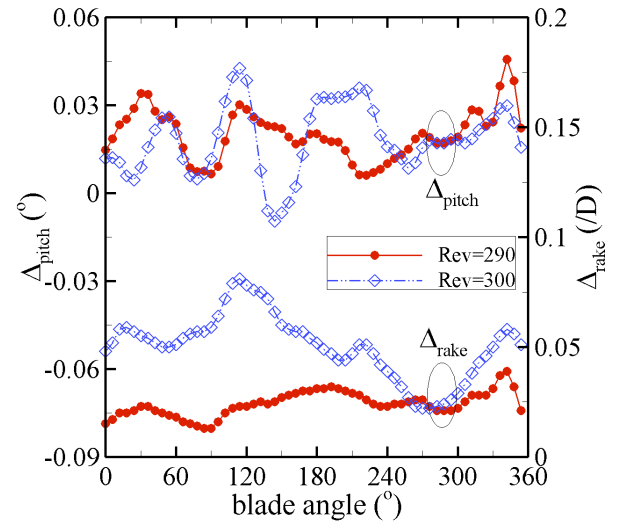


Figure 41. Predicted change in tip pitch angle and rake as a function of blade angles for  $t^*=290$  and  $t^*=300$  ( $J=-1.0$ ).

metry.

We have found that the flows over the blades are almost always a combination of attached and separated flows. The most common turbulent flow feature is leading edge separated flow caused by the sharp (and cambered) edge. The extent of the separations only covers a small portion of a blade, with the remainder of the blade having attached flow. The large force fluctuations are caused by larger separations, but these cannot be classified as massively separated. Thus, it may be prudent to ensure correct near wall behavior either with finer wall-normal grid spacing or wall models.

The transient surface pressures for these events have been applied as forcing functions to a finite element code. Results of the FE analysis show that this propeller undergoes tip deflection well within the material's plastic limit and that the highest strains occur near the blade root. This is a first step toward development of integrated fluid-structure interaction capability for crashback flows.

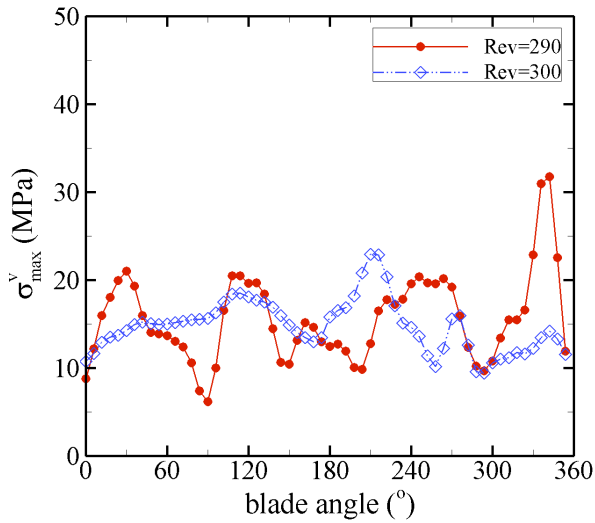


Figure 42. Predicted maximum von Mises stresses as a function of blade angles for  $t^*=290$  and  $t^*=300$  ( $J=-1.0$ ).

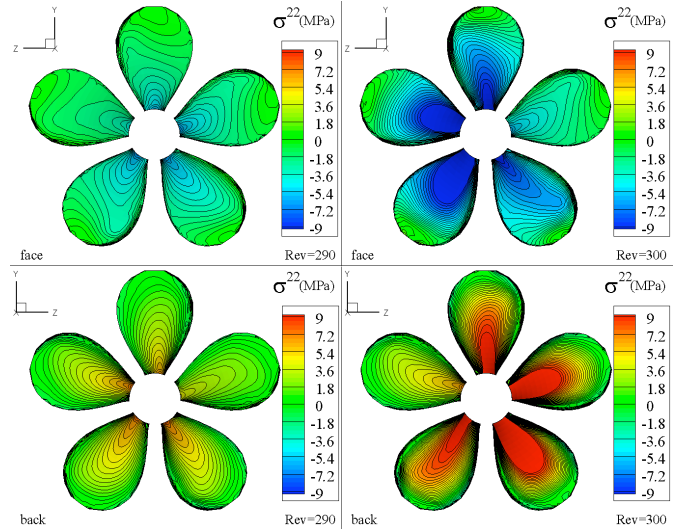


Figure 44. Predicted bending stress ( $\sigma^{22}$ ) contours at varying blade angles for  $t^*=290$  and  $t^*=300$  at  $J=-1.0$  (left-top: face side,  $t^*=290$ ; right-top: face side,  $t^*=300$ ; left-bottom: back side,  $t^*=290$ ; right-bottom: back side,  $t^*=300$ ).

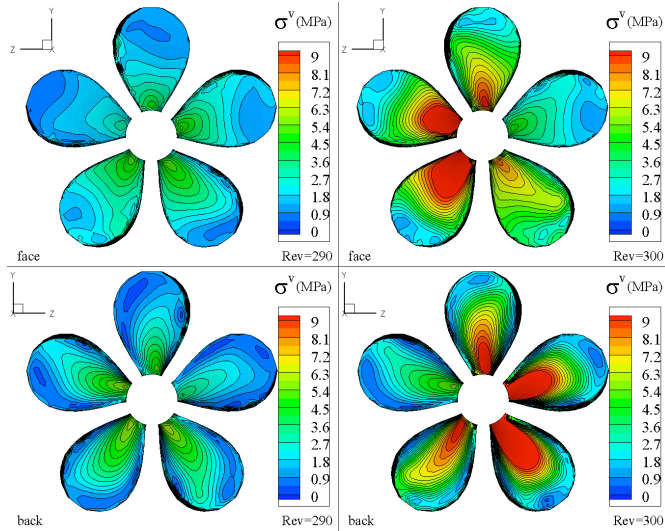


Figure 43. Predicted von Mises stress ( $\sigma^v$ ) contours at varying blade angles for  $t^*=290$  and  $t^*=300$  at  $J=-1.0$  (left-top: face side,  $t^*=290$ ; right-top: face side,  $t^*=300$ ; left-bottom: back side,  $t^*=290$ ; right-bottom: back side,  $t^*=300$ ).

## 5 RECOMMENDATIONS

We hypothesize that the difference between the OW and VPWT data is caused by the location of the propeller shaft — downstream for the OW tests and upstream for the VPWT test. A simulation of the OW configuration would be instrumental in proving this hypothesis.

This paper represents only a nascent attempt at correlating the flow, pressures and structural response. A more careful study

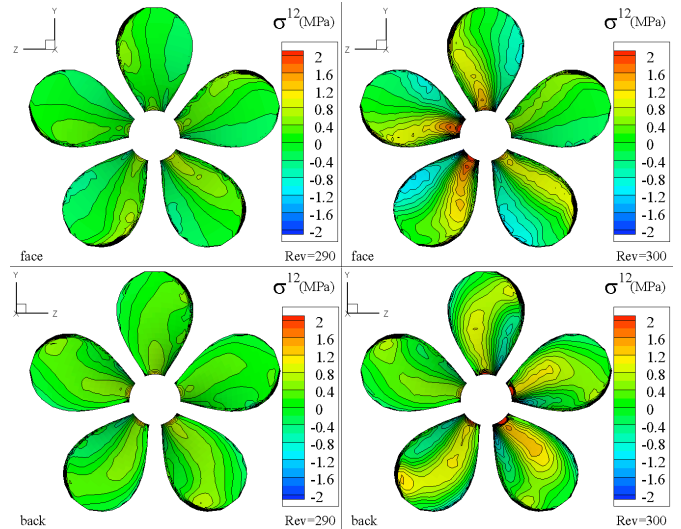


Figure 45. Predicted shear stress ( $\sigma^{12}$ ) contours at varying blade angles for  $t^*=290$  and  $t^*=300$  at  $J=-1.0$  (left-top: face side,  $t^*=290$ ; right-top: face side,  $t^*=300$ ; left-bottom: back side,  $t^*=290$ ; right-bottom: back side,  $t^*=300$ ).

with exact correlations between flow and structural responses would allow us to determine the types of flows responsible for the highest loadings, thus helping to improve our knowledge of the optimal simulation methodology.

## ACKNOWLEDGMENT

This work was funded by Office of Naval Research (Dr. Ki-Han Kim) under NSWCDD work unit 07-1-5400-300, ONR order numbers N0001407WX20771/AA, N00014-05-1-0694 and N00014-07-1-0491. The encouragement and advice of Drs. Joseph J. Gorski, Joseph Slomski and Sung-Eun Kim is duly acknowledged. We would also like to thank Drs. Stuart Jessup, David Fry, Martin Donnelly, and Joel Park, Don Fuhs, Steve Neely, and Thad Michael for their assistance with the experimental data reduction and insights. We would also like to thank Mr. Larry Mulvihill in his assistance running the LES simulations. The LES simulations were run on the NSWCDD SeaTech Center's SGI Altix computer "aspen." We would like to thank the staff at the Seatech Center for their support, in particular Mr. William Smith who helped develop the Ensignt data server-of-servers data output software.

## REFERENCES

- [1] Abaqus version 6.5 documentation. Technical report, Abaqus, Inc.
- [2] P. Atkinson and E.J. Glover. Propeller hydroelastic effects. In *Propellers '88 Symposium*. SNAME, 1988.
- [3] David H. Bridges. A detailed report of the flowfield of a submarine propeller during a crashback maneuver. Technical Report MSSU-ASE-04-01, Mississippi State University, Aug 2004.
- [4] Peter A. Chang, Michael P. Ebert, Krishnan Mahesh, and Jeremy Shipman. Prediction of high amplitude forces during propeller crashback. In *DOD High Performance Computing Modernization Program 2008 Users Group Conference*, page 11, Seattle, WA, 2008.
- [5] Massimo Germano, Ugo Piomelli, Parviz Moin, and William H. Cabot. A dynamic subgrid-scale eddy viscosity model. *Physics of Fluids A - Fluid Dynamics*, 3(7):1760–1765, 1991.
- [6] Van Emden Henson and Ulrike Meier Yang. Boomeramg: a parallel algebraic multigrid solver and preconditioner. *Applied Numerical Mathematics*, 41, 2002.
- [7] Jinhee Jeong and Fazle Hussain. On the identification of a vortex. *Journal of Fluid Mechanics*, 285:69–94, 1995.
- [8] Stuart Jessup, Chris Chesnakas, David Fry, Martin Donnelly, Scott Black, and Joel Park. Propeller performance at extreme off design conditions. In *25th Symposium on Naval Hydrodynamics*, St. Johns, Newfoundland and Labrador, Canada, 2004.
- [9] Stuart Jessup, David Fry, and Martin J. Donnelly. Unsteady propeller performance in crashback conditions with and without a duct. In *26th Symposium on Naval Hydrodynamics*, Rome, Italy, 2006.
- [10] C.-W. Jiang, R. Dong, H.-L. Liu, and M.S. Chang. 24-inch water tunnel flow field measurements during propeller crashback. In *21st Symposium on Naval Hydrodynamics*, Trondheim, Norway, 1996. National Academy Press.
- [11] J. Kuo and W. Vorus. Propeller blade dynamic stresses. In *10th Ship Technology and Research (STAR) Symposium*, 1985.
- [12] Y.J. Lee and C.C. Lin. Optimized design of composite propeller. *Mechanics of Advanced Materials and Structures*, 11(1):17–30, 2004.
- [13] D.K. Lilly. A proposed modification of the germano subgrid-scale closure model. *Physics of Fluids A*, 4(3):633–635, 1992.
- [14] C.C. Lin and Y.J. Lee. Stacking sequence optimization of laminated composite structures using genetic algorithm with local improvement. *Composite Structures*, 63(3-4):339–345, 2004.
- [15] G. Lin. Comparative stress-deflection analyses of a thick-shell composite propeller blade. Technical Report DTRC/SHD-1373-01, DTRC, Dec 1991.
- [16] G. Lin. Three-dimensional stress analysis of a fiber-reinforced composite thruster blade. In *Symposium on Propellers/Shafting*. SNAME, 1991.
- [17] H.J. Lin and J.J. Lin. Nonlinear hydroelastic behavior of propellers using a finite-element method and lifting surface theory. *Journal of Science and Technology*, 1:114–124, 1996.
- [18] H.J. Lin and J.F. Tsai. Analysis of underwater free vibrations of a composite propeller blade. *Journal of Reinforced Plastics and Composites*, 27(447):13, 2008.
- [19] Krishnan Mahesh, George S. Constantinescu, and Parviz Moin. A numerical method for large-eddy simulation in complex geometries. *Journal of Computational Physics*, 197:215–240, 2004.
- [20] K.S. Majety. *Solutions to the Navier-Stokes Equations in Non-Inertial Reference Frame*. PhD thesis, Mississippi State University, 2003.
- [21] Scott A. Slimon and Craig A. Wagner. Crashback maneuvers. In *DoD HPCMP Users Group Conference 2007*, pages 433–439, Pittsburgh, PA, 2007.
- [22] S. Thangam, X. Wang, and Y. Zhou. Development of a turbulence model for flows with rotation and curvature. In Manuel D. Salas, Jerry N. Hefner, and Leonidas Sakell, editors, *Modeling Complex Turbulent Flows*, volume 7 of *ICASE/LaRC Interdisciplinary Series in Science and Engineering*, pages 361–372. Kluwer Academic Publishers, Dordrecht, The Netherlands, 1999.
- [23] Martin Vysohlid and Krishnan Mahesh. Large eddy simulation of crashback in marine propellers. In *44th AIAA Aerospace Sciences Meeting and Exhibit*, Reno, NV, 2006.
- [24] Martin Vysohlid and Krishnan Mahesh. Large eddy simulation of crashback in marine propellers. In *26th Symposium on Naval Hydrodynamics*, Rome, Italy, 2006.
- [25] Yin L. Young. Time-dependent hydroelastic analysis of

cavitating propellers. *Journal of Fluids and Structures*, 23:269–295, 2007.

- [26] Yin L. Young. Fluid-structure interaction of flexible composite marine propellers. *Journal of Fluids and Structures (online)*, 2008.